Theses and Dissertations

2017

Coarse Grain Molecular Model Development and Implementation for Describing von Willebrand Factor Behavior in Human Blood Flow

Wei Wei
Lehigh University

Follow this and additional works at: https://preserve.lehigh.edu/etd

 Part of the Mechanical Engineering Commons

Coarse Grain Molecular Model Development and Implementation for Describing von Willebrand Factor Behavior in Human Blood Flow

by

Wei Wei

A Dissertation

Presented to the Graduate and Research Committee

of Lehigh University

in Candidacy for the Degree of

Doctor of Philosophy

in

Mechanical Engineering

Lehigh University

August 2017

Approved and recommended for acceptance as a dissertation in partial fulfillment of the requirements for the degree of Doctor of Philosophy

Name: Wei Wei

Dissertation Title: Coarse Grain Molecule Model Development and Implementation for Describing von Willebrand Factor Behavior in Flow Conditions

_____
Defense Date

_____
Dr. Alparslan Oztekin, Dissertation Director, Chair

_____
Approved Date

Committee Members:

_____
Dr. Edmund Webb III

_____
Dr. Xuanhong Cheng

_____
Dr. Xiaohui (Frank) Zhang

ACKNOWLEDGEMENTS

This dissertation would not have been possible without so many people. I have been extremely lucky to have not one but two great advisors. I would first like to thank Dr. Alparslan Oztekin and Dr. Edmund Webb III for their solid support, patient guidance and tremendous help. They have been mentors, colleagues and friends. I would also like to thank my committee members Dr. Xiaohui (Frank) Zhang and Dr. Xuanhong Cheng for their inspiring comments and generous help of experimental studies.

Great friends I made at Lehigh were helpful in getting through some of the emotional moments. Yang Chen, I-Han Liu, Haolin Ma and Guosong Zeng became good friends and sharing both happiness and sadness of the life. I want to thank Chuqiao Dong, Dr. Baiou Shi, Michael Morabito and Weizhou Zhou for making the office full of fun. Thanks also goes to Dr. Yan Xu, Dr. Wei Zhang, Dr. Matthew Dragovich for teaching me how to operate experimental equipment; Wenpeng Cao and Whitney Lei for preparing the samples.

I would also like to thank my parents, Luguang Wei and Ling Liang, for all their love, encouragement and support. Although unsure of what I am really working on, they are always there for me.

Thank Lehigh for all the memories.

TABLE OF CONTENTS

LIST OF TABLES

LIST OF FIGURES

ABSTRACT

von Willebrand Factor (VWF) is a large multimeric protein which is very important for the hemostasis of bleeding blood vessels. Critical steps in the process are the accumulation and aggregation of platelets at the damaged vessel wall, forming hemostatic plugs. Near injury sites, hydrodynamic force in the bloodstream elongates VWF with a sharp increase, exposing binding sites for platelets and collagen. Flow-induced conformational change of VWF regulates its binding to clotting agents in the blood.

A coarse grain molecular model is proposed for the VWF multimer that incorporates observed mechanical properties of VWF monomers. In this model, each monomer is represented by a finitely extensible nonlinear elastic (FENE) spring connecting two beads. A2 domains are represented by the FENE spring because the A2 domain, similar to FENE springs, permits extensive elongation with an applied force. The beads at each end of the spring represent relatively rigid domains adjacent to A2 in VWF monomers. Adjacent monomers are connected by a stiff harmonic spring to form VWF multimers in the model. VWF multimers represented by this model have been studied to understand the conformational change of a single VWF multimer in response to shear flow. Fluctuations in model A2 domains were shown to increase significantly at high flow, including periodic complete extension of the domain.

After validating our model in normal flow scenario, we extend this study further to the binding between VWF and collagen. To investigate VWF binding to collagen that is exposed on injured arterial surfaces, Brownian dynamics simulations are performed with a coarse-grain molecular model. Accounting for hydrodynamic interactions in the presence of a stationary surface, shear flow conditions are modeled. Binding between beads in

coarse-grain VWF and collagen sites on the surface is described via reversible ligand-receptor-type bond formation, governed via Bell model kinetics. For conditions where binding is energetically favored, the model predicts a high probability for binding at low shear conditions; this is counter to experimental observations but in line with what prior modeling studies have revealed. To address such discrepancies, an additional binding criterion is implemented that depends on the conformation of a sub-monomer feature in the model, local to a given VWF binding site. The modified model predicts shear-induced binding, in very good agreement with experimental observations; this is true even for conditions where binding is significantly favored energetically. Biological implications of the model modification are discussed in terms of mechanisms of VWF activity.

Experimental work that investigates the properties of individual VWF molecules guided the parameters in computational study. Within this dissertation, optical tweezers are employed to study the A2-domains of VWF. Such a direct experimental method performs very precise measurement on the most fundamental properties of VWF molecules (such as force/extension behavior). This experimental method achieves great resolution and sensitivity in real time. Experimental results unveil the mechanism of VWF unfolding, contributing to the current coarse grain model development, and giving us the ability to model abnormal VWF molecules.

To our knowledge, this coarse grain molecular model is the only model to render sub-monomer units of VWF and it is capable of capturing sub-monomer dynamical behavior. By introducing an additional degree of freedom, our model successfully characterizes many of the flow-induced mechanical mechanisms exhibited by VWF, such as shear-induced conformational changes and unfolding phenomena. Further, our model

2

captures shear-induced VWF-collagen binding behavior in situations where binding is highly favorable, which had previously not been obtained in the literature.

CHAPTER 1 *Introduction*

1. Motivation - von Willebrand Factor (VWF) and von Willebrand Disease(VWD)

In human body, bleeding is stopped by forming a clot at the site of vascular damage. Critical steps in the process are the accumulation and aggregation of platelets at the damaged vessel wall, forming so called platelet "plugs". (1) Under rapid flow condition such as in arteries and arterioles, however, platelets cannot adhere themselves to vessel walls due to the strong hydrodynamic force imposed by the flowing fluid. In such scenarios the plasma protein, von Willebrand Factor (VWF) plays an indispensable role in sticking to both platelets and vessel wall, allowing the formation of platelet plugs. (2, 3) Ultra-long VWF multimer, which is released from Weibel-Palade bodies (WPB), is cleaved by ADAMTS13 (a disintegrin and metalloprotease with a thrombospondin type 1 motif, member 13) into smaller fragments with a wide range of size distributions. (4–7) After cleavage, physiological functional VWF contain from 40 to 200 monomers such that molecules can be extended to tens of microns in flow. (8) Along its length, VWF carries binding sites for both platelets and collagen, but only few are exposed to the blood flow when VWF is in a globular state. Once VWF transforms from a globular state to an elongated state, more binding sites are exposed and thus the unfolding of VWF enables itself to achieve better hemostatic performance. (9) However, the protease vWF size is important in hemostasis. (10) Functional imbalance in multimer size can cause microvascular thrombosis or bleeding. Put simply, if too small, VWF cannot properly

initiate clotting; if too large, VWF may initiate clotting in undesired (i.e. otherwise healthy) scenarios.

In the past few decades, there has been a steadily growing interest in the study on von Willebrand Factor (VWF) because of its importance in coagulation. One in 100 individuals in United States has functional defects or no/low expression of VWF. The obvious symptoms are usually in the form of easy bruising, nosebleeds, bleeding gums, heavy menstrual periods, and blood loss during childbirth. Based on the clinical observation and pathology studies, usually hereditary von Willebrand Disease (VWD) are categorized into one of three types: VWD Type 1, VWD Type 2, and VWD Type 3. Within each of these three main types of VWD, there are various subtypes. (2, 11, 12) With the development in diagnostic techniques, more new subtypes have been reported. However, the therapeutic solution to cure VWD has not been fully established. Currently, the main treatment for severe VWD patients is still using the plasma infusion method. Blood products can never be risk-free. Major risk of transfusion-transmitted method includes hemolytic reactions and bacterial infection. Transfused plasma can also affect patients' immune system.

In December 2015, the U.S Food and Drug Administraion (FDA) approved the first recombinant VWF treatment, VONVENDI. VONVENDI replaces the deficient VWF in the body of VWD patients, and mainteins a functional level of concentration for 72 hours. This new treatment is approved for on-demand treatments and controls bleeding episodes in adults diagnosed with VWD. VONVENDI doesn't contain any raw human or animal material, which eliminates the risk of blood-borne infection. In clinic studies, VONVENDI shows treatment success: most of mild bleeding episodes and two-thirds of moderate

bleeding episodes were controlled with a single dose. Severe bleedings was controlled with 2 to 4 infusions. (13) The success of recombinant VWF treatment is a milestone in VWD research and treatment. However, the mechanisms of VWF function are still not fully understood.

Research shows that VWF multimers act as a flow sensor, responding to strong hydrodynamic forces by changing conformation. (14) In 1990s, Perkins and co-workers detected conformational change of single DNA molecules under a flow. (15) The fluctuating chain was imaged have a cone-like envelope and shows a sharp increase in intensity at the free end. Similar phenomena, as shown in Fig. 1(b), has been observed with VWF, which changes conformation under a certain shear rate and becomes unfolded.
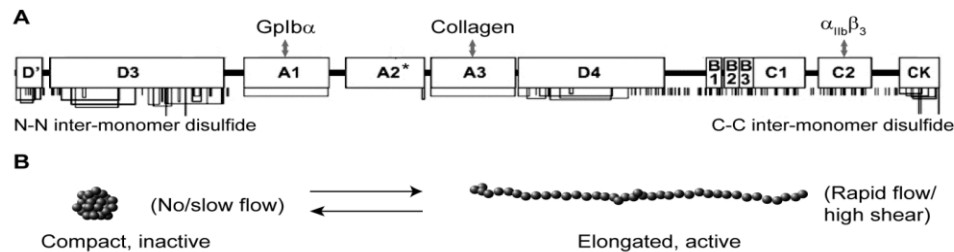
Figure 1 (a) Schematic illustration of VWF's domain arrangement. (b) Possible mechanism of flow-induced conformational change. VWF is a long multimer containing up to 200 monomers. In the image above, each monomer is modeled as sphere.

Because of its unique behavior under flow, VWF has potential application as a vehicle for targeted drug delivery. Drug-loaded VWF maintains a globule state until it is exposed to abnormal blood flow conditions, such as in a bleeding site, and unfolding of VWF leads to drug release. Such targeted therapy may improve drug potency at the site in need and decrease toxicity in circulation. The exact mechanism how VWF senses flow by presumably switching between the two conformations is still elusive. Molecular dynamics simulation can help study the mechanism of flow induced conformational change in

biopolymers and attain a clearer picture of how VWF molecules achieve flow sensing at a single molecule level.

2. Structure and Functionality of Von Willebrand Factor

Pro-VWF (VWF precursor) has a molecular weight of about 350 kDa. Each monomer has five types of structural domains that are arranged in the sequence D1-D2-D'-D3-A1-A2-A3-D4-B1-B2-B3-C1-C2-CK. When a blood vessel is injured, the D1 and D2 domains are cleaved by furin, the prodomain remains strongly associated and the VWF monomer now is in its mature form (Fig.1 (A)). (16) VWF monomers dimerize through the CT domain. The dimers are connected through disulfide bonds in the D'-D3 domain to form a mutimeric structure. Because of lacking a long-range disulfide bond, the A2 domain can be completely unfolded by elongational force such as viscous force due to shear flow and/or elongational flow. A1 domain has strong interactions with platelet glycoprotein Ib (GPIB). Similar to A2 domain unfolding, studies on interactions between A1 domain and GPIb suggest a force-induced conformational change. (16–19) Interestingly, unfolding of the A2 domain as it becomes susceptible to scission by ADAMTS13 and activation of the A1 domain for binding to platelet glycoprotein Ib (GPIB) are both induced by high flows, but binding to GPIb occurs more rapidly. (16) Collagen binds to the A3 domain that bears the β3-strand. VWF binding on collagen is mainly triggered by its conformational change. (20) Once the shear rate of the flow is larger than certain threshold, VWF multimer undergoes tremendous conformational change and exposes A3 domains for binding to collagen and A1 domains for binding to platelets via GPIb.

3. Molecular Dynamics Model for Von Willebrand Factor

In what follows, all discussion on molecular scale simulation focuses on classical techniques, which do not explicitly resolve electronic degrees of freedom; there is no discussion on quantum techniques, which do resolve electronic degrees of freedom to varying degree, depending on the specific technique. The focus on classical techniques is because the time and length scales of molecular phenomena being explored here are inaccessible to quantum mechanical based techniques. Molecular dynamics (MD) simulation is one of the main molecular simulation techniques. It has been widely used for understanding the chemical and physical properties of different materials. (21) In MD simulation, equations of motion are solved as a function of time, generating the microscopic states of the system. Thus, MD has the ability to capture the relaxation of a system to equilibrium by providing the time scale. (22) MD simulation in polymers requires connecting models at different length and time scales. Various levels of details can be observed with different sub-models while simulations still maintain the major interested feature of the polymer chain. On the atomic level, an explicit atom model considers all atoms including hydrogen as separate interaction sites, providing most detailed information on both the polymer and solvent. A united atom model reduces degrees of the freedom in the explicit model by combining a group of atoms into one unit (i.e. a coarse-grain unit called a united atom); this is a good approximation with less computation time when specific chemistry information need not be represented (e.g. when the intermolecular motion is much more important than the intramolecular binding). (21) A coarse-grain approach reduces the complexity and computation time of the system even

further by truncating the polymer into small sub-groups which can be one atom, a few united atoms, monomers or even the whole chain. Again, the efficacy of such models is dependent upon the specific property of interest: when bond formation energy is critical, all classical techniques may be insufficient and quantum techniques may be required; on the other hand, when macromolecular elongation and elongation-induced binding are of interest, any form of explicit atom technique is too computationally expensive and, arguably, unnecessary. The latter example described is similar to interests here and is ideally suited for investigation via coarse-grain molecular methods. Accordingly, in this dissertation research, a coarse-grain model is adopted for its computationally efficiency and it will be shown herein to provide highly satisfying agreement with available experimental data.

A Gaussian chain model is the simplest coarse-grain model for polymer simulation, which allows an indefinite extension when increasing shear rate or other force. The freely-jointed chain (FJC), introduced by Peterlin in 1966, is a modification of Gaussian model. (23) The real chain is replaced by a set of points connected by rigid rods of fixed length. Kratky and Porod modified the Gaussian model for the worm-like chain (WLC). (24) In this model, beads are connected by flexible, inextensible rods, which have fixed length; it is usually used to describe helical structures. The bead-spring chain model replaces rods in FJC and WLC by completely flexible springs, and it is also called a "Rouse model". (25) This model is the simplest idealization of a polymer molecule that captures the essential physics required to simulate polymer dynamics. It considers a linear relationship between the polymer chain extension and force, such as the Hookean Spring. Hydrodynamics interaction (HI) has been found important when two or more particles move in a viscous

fluid because it governs the dynamics of colloidal suspensions. (26) In basic terms, HI refer to the fact that an entity in a fluid disturbs the fluid with its motion, thereby affecting how the fluid influences another entity some distance away from the first. The Rouse model is not suitable for dilute polymer solutions as HI is neglected. Zimm performed the first calculation of the linear viscoelastic spectrum of the bead-spring chain with HI. (27) Alexander-Katz et al (28, 29) and Rudisill et al (30) further examined the behavior of a single polymer by bead-spring model with HI, and confirmed that HI is very important to accurately model the dynamics of polymer. Sing and co-workers utilized a similar model but included vWF-collagen adhesion by Bell model interactions. (31) They showed that vWF molecule interacts with the surface and the pathways for unbinding from the surface is suppressed due to lift force and/or rolling pathways, which matched the observation from experiments by Schneider et al(32). Such lift forces are only properly predicted if HI is included in the simulation (including necessary algorithm modifications for simulations of molecules flowing near a stationary surface).

In the classical coarse-grain model, one VWF monomer is treated as one bead by neglecting all intramonomer interaction. This simulation technique has been shown to be very efficient, especially for modeling long biopolymer chains under complex flow conditions. (33–36) However, experimental research has shown that different domains of VWF may be functionalized differently. Zhang et al. characterized the unfolding of A2 domain by single molecule force spectroscopy. (37) Other research suggested that intramolecular interaction of VWF may change its functionality, depending on the conformation of sub-monomer units. For example, it has been shown that VWF/platelet adhesion is inhibited due to A1 domain being shielded by D'D3 domains or A2 domains

until sufficient elongational force essentially pulls those other domains out of the way of the A1 domain/platelet interaction. (38–40) Thus, in this study, we established a new coarse-grain model that has the capability to simulate a greater degree of intramonomer interaction by treating one monomer with two beads connected by a finite extendable nonlinear elastic (FENE) spring; the spring is representative of the extensible A2 domain and each bead represents a collection of domains on either side of the A2 domain in a VWF monomer. By introducing an additional degree of freedom, this coarse grain molecular model, which will be presented in a later section, successfully characterizes many of the mechanisms exhibited by VWF - such as shear-induced conformational changes, unfolding phenomena, and VWF-collagen binding behavior.

CHAPTER 2 *Von Willebrand Factor Simulation Methodology*

1. Introduction

As mentioned in Chapter 1, coarse-grain molecular modeling is one of the major simulation techniques that has been widely used to understand macromolecule behavior. Unlike atomic level models, a coarse-grain model collapses (or coarse-grains) multiple atoms into a single entity (typically a spherical particle but aspherical particle models have been advanced); these particles are often called beads whose dynamic behavior is described by Newton's law. While unable to address some questions rooted in atomic scale behavior, coarse-grain models are designed to capture the most relevant features of behavior at the atomic level that govern macromolecular interaction and dynamics. To achieve this, a balance needs to be struck between providing more accurate details and consuming less computational power. Generally, a good coarse-grain model requires good chosen procedure, including: (41) a) the model resolution (how many atomic particles per coarse-grain bead), b) the mapping procedure (what each coarse grain bead represents), c) the potential energy function between beads (and sometimes between springs connecting beads), and d) coarse grain model parameters optimized with experimental studies and/or higher fidelity atomic level simulations. Each component of this procedure is discussed in greater detail in the following section.

2. Coarse-grain Model Chosen Procedure

2.1. Model resolution

A typical classical coarse-grain model treats a biopolymer as beads connected by springs (i.e. a bead-spring model). The simplest realization of a bead-spring model is to consider a polymer as the combination of one harmonic spring connecting two beads, known as the Dumbbell Model. (42) Dumbbell model replaces the whole polymer chain by a single spring, captures the important physics: chain flexibility and drag due to solvent. It is widely used, but the simple Dumbbell model is not sufficient to properly describe the conformational change of larger polymers, especially under imposed flow fields. (14, 25) Such detail requires higher model resolution, which leads to multiple beads connected with multiple springs. Typically, one bead representing one monomer is sufficient to study intermolecular interactions and resultant macromolecular dynamic behavior. However, as mentioned in Chapter 1, intramolecular interaction is also very important in the study of VWF. Thus, we increased the resolution in the model presented here: two beads connected by a FENE spring represent one monomer; further, parameters in the model here were – in all ways possible – guided by experimental data.

2.2. Model mapping procedure

VWF has extremely complicated structure largely due to its various domains performing distinct functions. Among all the domains, A2 domain is a force-sensitive domain that lacks disulfide bonds and thus can be unfolded by external stretching forces, such as the drag force due to shear or elongational flow. (16) The A3 domain is a bridge between VWF and exposed collagen of sub-endothelial matrix when the vessel is injured, which make A3 domain essential for collagen binding. (43) Although A1 domain also has been reported to bind to collagen fibers, A3-collagen binding is considered to be dominant.

(44) A1 domain mainly binds with platelet glycoprotein Ib (GPIb), which is the receptor on membrane of platelet. Notably, the binding between A1 domain and platelet is not included in this study. Nonetheless, it is useful to point out that recent experimental data provide strong evidence that A1/platelet binding is inhibited by the adjacent A2 domain such that facile binding is only observed when the adjacent A2 domain is partially elongated.

To map a VWF monomer onto elements of a coarse-grain model, a FENE spring is adopted to describe the extensible regions or A2 domain of the monomer. Two spherical beads at each end of the spring model collections of relatively more rigid domains on either side of the A2 domain (Fig. 2 (B)). As such, one of the two beads contains the A3 domain (shaded in Fig. 2(B)) and the other contains the A1 domain; again, this dissertation research did not explore A1/platelet binding and is instead focused on behavior of the A3 domain near exposed collagen. Thus, only the bead containing the A3 domain on each monomer is capable of binding to model collagen sites. Multimers are modeled by connecting monomers with a harmonic spring, which is relatively stiff. Fig. 3 is a schematic illustration of a 25-mer VWF chain with examples of different conformations of VWF chain. White beads represent the left bead in Fig. 2 (B), while black beads represent the shaded bead with collagen binding site. Note in the Fig. 3 images that, as is experimentally observed for VWF, adjacent monomers bind in a head-to-head, tail-to-tail sequence.
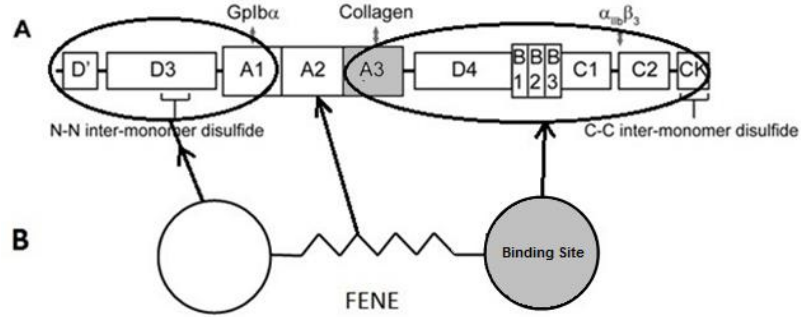
Figure 2 (A) Schematic illustration of vWF's domains. (B) The VWF monomer model containing two rigid beads connected by a highly flexible FENE spring.
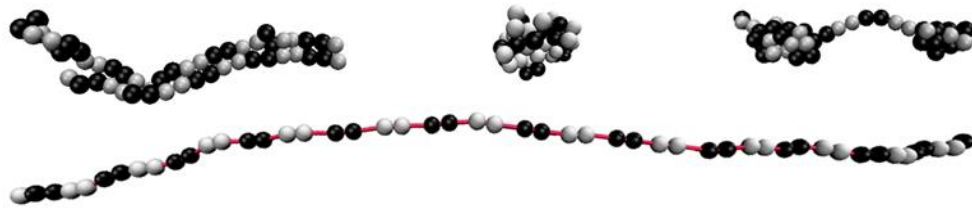
Figure 3 Schematic illustration of vWF multimer.

2.3. Physical forces and phenomena

Over the range of length scales and time scales of coarse-grain VWF model, the following effects are of primary significance, approximately ordered based on their importance: (45) (a) Viscous drag; (b) Entropic elasticity; (c) Brownian forces; (d) Hydrodynamics interaction (HI); (e) Excluded-volume interactions; (f) Internal viscosity, and (g) Self-entanglement. Viscous drag is the frictional force due to solvent exerting on the polymer, which is always very important regardless what flow condition. Entropic elasticity becomes important when the flow is strong enough to change the conformation of the chains from their equilibrium states. Due to the collision on the polymer with solvent particles, Brownian motion also effects the conformation. HI is the phenomena that the

17

flow field perturbed by one particle that influences the drag on other particles, which is reported to be essential in this coarse grain model. (45, 46) Excluded-volume interactions present the repulsion between beads that prevent their overlap, which can be neglected in some solvent condition under their theta temperature, at which the repulsion is weak enough compared with the effect of the solvent. (47) The last two interaction have not been proved to have any important influence, and thus will not be included in this study.

The governing equations for a system with N beads in the inertia free limit are obtained by a force balance on each bead,

$$\boldsymbol{F}_i^D + \boldsymbol{F}_i^S + \boldsymbol{F}_i^{In} + \boldsymbol{F}_i^B + \boldsymbol{F}_i^W + \boldsymbol{F}_i^C = 0, \quad i = 1,2,\dots,N \tag{1}$$

where the subscript i refers to the bead number and $\boldsymbol{F}_i^D$, $\boldsymbol{F}_i^S$, $\boldsymbol{F}_i^{In}$, $\boldsymbol{F}_i^B$, $\boldsymbol{F}_i^W$ and $\boldsymbol{F}_i^C$ are the hydrodynamic (viscous) drag force, the spring force (either FENE or harmonic), the interaction force between beads, the Brownian force, the wall force, and the A3 domain - collagen binding force, respectively.

2.3.1. Viscous drag force

The hydrodynamic drag force on bead i is given by,

$$\boldsymbol{F}_i^D = -\zeta(\dot{\mathbf{r}}_i - \boldsymbol{v}_i) \tag{2}$$

where ζ is the drag coefficient, $\mathbf{r}_i$ is the position vector, $\dot{\mathbf{r}}_i \equiv \frac{d\mathbf{r}_i}{dt}$ is the velocity of the bead i , $\boldsymbol{v}_i$ is the velocity field. In the absence of HI, $\boldsymbol{v}_i$ is undisturbed and is simply the transpose of the velocity gradient tensor; i.e., $\boldsymbol{v}_i = (\nabla \boldsymbol{u})^T \mathbf{r}_i$, so that the drag force for free draining (FD) case has the form

$$\boldsymbol{F}_i^D = -\zeta(\dot{\mathbf{r}}_i - (\nabla \boldsymbol{u})^T \mathbf{r}_i) \tag{3}$$

Substituting Eq. (3) into Eq. (1) and rearranging gives

$$\dot{\mathbf{r}}_i = (\nabla \boldsymbol{u})^T \mathbf{r}_i + \frac{1}{\zeta}\left(\boldsymbol{F}_i^S + \boldsymbol{F}_i^{In} + \boldsymbol{F}_i^B\right) \qquad (4)$$

which is the generic form of a Langevin equation. To account for HI using the bead-spring model, disturbed flow field produced by forces that each bead exerts on the solvent must be considered to correct the velocity acting on all other beads. (45) The velocity, $\boldsymbol{v}_i$ in Eq. (1) should include an additional term, a disturbed velocity $\boldsymbol{v}'_i$, which produced by another bead j and it is a linear function of the hydrodynamic drag force on bead j, so that $\boldsymbol{v}'_{ij} = -\boldsymbol{\Omega}_{ij} \cdot \boldsymbol{F}_j^D$. Based on Newton's second low, the hydrodynamic drag force of bead j, $\boldsymbol{F}_j^D$, is equal and opposite to the nonhydrodynamic forces (i.e. spring forces, intramolecular forces, Brownian forces… etc.), thus $\boldsymbol{F}_j^D = -\left(\boldsymbol{F}_j^S + \boldsymbol{F}_j^{In} + \boldsymbol{F}_j^B + \boldsymbol{F}_j^W + \boldsymbol{F}_j^C\right)$. Substituting gives

$$\boldsymbol{v}'_{ij} = -\boldsymbol{\Omega}_{ij} \cdot \boldsymbol{F}_j^D = \boldsymbol{\Omega}_{ij} \cdot \left(\boldsymbol{F}_j^S + \boldsymbol{F}_j^{In} + \boldsymbol{F}_j^B + \boldsymbol{F}_j^W + \boldsymbol{F}_j^C\right) \qquad (5)$$

where the HI tensor $\boldsymbol{\Omega}_{ij}$ is a function of the separation distance between beads i and j. Notably, $\boldsymbol{v}'_{ij}$ here only represents the disturbance on bead i due to bead j, thus the total disturbance on bead i should be $\sum_{j=1}^{j=N} \boldsymbol{v}'_{ij}$. More detailed discussion on HI can be found in the following section.

2.3.2. Hydrodynamic interaction

Particles moving in a viscous field induce a flow field around themselves which will be felt by all other beads. (26) In other words, hydrodynamic forces are transmitted between the particles in the form of translations and rotations, and the motions of particles are coupled through the flow field around (Fig. 4 (A)). Also, particles on the surface of a

cluster are shielding the ones inside, which leads to the situation that inside particles feel less hydrodynamic drag force from the flow field (Fig. 4 (B)).
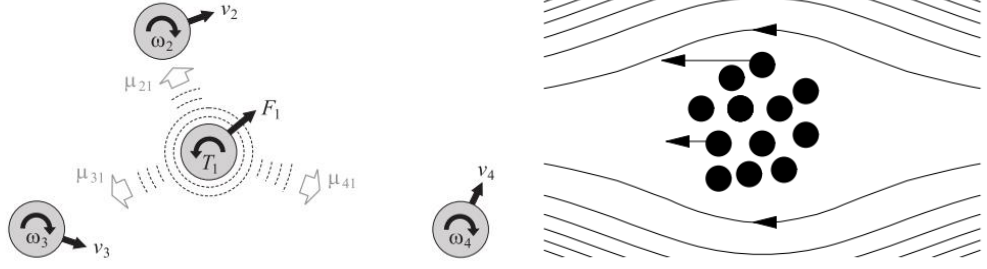
Figure 4 A) Particles subject to external forces due to the movement of other beads. (26) **B) Particles inside a cluster experience a smaller drag force than those on surface.** (48)

As mentioned in early sections, HI is always important for long polymer molecules with large molecular weight. Ermak and McCammon et al (49) had shown that the disturbance velocity can be included into the Langevin equation by introducing the diffusion tensor $\mathbf{D}_{ij} = \frac{k_B T}{\zeta}\left(\delta_{ij}\mathbf{I} + \zeta\mathbf{\Omega}_{ij}\right)$, where k_B is Boltzmann's constant, T is absolute temperature, δ_{ij} is the Kronecker delta and $\mathbf{I}$ is an unit tensor. $\mathbf{D}_{ij}$ is itself a second-order tensor, i.e., 3×3. Notably, the overall diffusion tensor $\mathbf{D}$ is force-order tensors, which means the dimension of it is $3N \times 3N$ for a N-beads system.

In general, calculating the diffusion tensor $\mathbf{D}$ is complicated because it is related to the instantaneous positions of all beads in a nonlinear way. (50) In polymer modeling, the diffusion matrix is often approximated by its far-field asymptotes. (51) The lowest order of approximation is the Oseen-Burgers (OB) tensor (14, 52, 53),

$$\mathbf{D}_{ii} = \frac{k_B T}{6\pi\eta a}\mathbf{I}$$
$$\mathbf{D}_{ij} = \frac{k_B T}{8\pi\eta\, r_{ij}}\left(\mathbf{I} + \frac{\mathbf{r}_{ij}\mathbf{r}_{ij}}{r_{ij}^2}\right), \quad i \neq j$$

(6)

where $\mathbf{r}_{ij} = \mathbf{r}_i - \mathbf{r}_j$, and $r_{ij} = |\mathbf{r}_{ij}|$. When the distance between beads is less than the bead diameter, the tensor becomes nonpositive definite, which causes numerical unstable, and thus the Oseen-Burgers tensor becomes unsuitable for simulations. A better approximation is the Rotne-Prager-Yamakawa (RPY) tensor, which considers the finite size of the beads. There are two expressions in RPY tensor, one is for separation distances between beads is larger than twice the radius of the bead, and the other for separations less than this (beads are overlapping) (54, 55),

$$\mathbf{D}_{ii} = \frac{k_B T}{6\pi\eta a}\mathbf{I}$$

$$\mathbf{D}_{ij} = \frac{k_B T}{8\pi\eta}\frac{1}{r_{ij}}\begin{cases}\left[\left(1 + \frac{2a^2}{3r_{ij}^2}\right)\mathbf{I} + \left(1 - \frac{2a^2}{r_{ij}^2}\right)\frac{\mathbf{r}_{ij}\mathbf{r}_{ij}}{r_{ij}^2}\right], & r_{ij} \geq 2a \\ \frac{r_{ij}}{2a}\left[\left(\frac{8}{3} - \frac{3r_{ij}}{4a^2}\right)\mathbf{I} + \frac{r_{ij}}{4a}\frac{\mathbf{r}_{ij}\mathbf{r}_{ij}}{r_{ij}^2}\right], & r_{ij} < 2a\end{cases}, \quad i \neq j \tag{7}$$

As the ratio of the bead radius to the distance between beads becomes small, the RPY tensor can be reduced to the OB tensor. Note that the free draining (without HI) model always have undisturbed flow field, so that can be easily obtained with $\mathbf{D}_{ij} = \mathbf{D}_{ii}$ for all beads regardless their radius.

2.3.3. Spring force

Entropic elasticity is important when the flow is strong enough to stretch or shrink the chain, and the spring force represents such an effect. The spring force acts on two beads connecting has the same magnitude but different direction. Considering a chain of beads connected by springs and with each bead (other than the two ends) bound by two springs leads to the following

$$\mathbf{F}_i^S = \mathbf{F}_{Spring\_i}^S - \mathbf{F}_{Spring_{i-1}}^S \quad , \qquad 2 \leq i \leq N-1 \tag{8}$$

where $\mathbf{F}_{Spring\_i}^S$ is the force that acts on bead i by spring i, and bead on the other side of the spring i feels the same force but towards different direction, $-\mathbf{F}_{Spring\_i}^S$. Two end beads only connect to one spring, thus the expressions for the ends are $\mathbf{F}_1^S = \mathbf{F}_{Spring\_1}^S$ and $\mathbf{F}_N^S = -\mathbf{F}_{Spring\_(N-1)}^S$. As mentioned previously, FENE springs represent A2 domains of VWF molecule while harmonic springs connecting VWF monomers. Here, $\mathbf{F}_{Spring\_i}^S$ is either a FENE spring force or a harmonic spring force. Most flexible synthetic polymers as well as single stranded DNA are modeled using the FENE spring law

$$\mathbf{F}_{FENE}^S = \frac{H\mathbf{Q}_i}{1 - Q^2/Q_0^2} \tag{9}$$

where H is the spring constant, $\mathbf{Q}_i = \mathbf{r}_{i+1} - \mathbf{r}_i$, Q is the magnitude of $\mathbf{Q}_i$ and Q_0 is the maximum extended length for the spring. The expression for the harmonic spring is given by

$$\mathbf{F}_{Harmonic}^S = k\frac{\mathbf{Q}_i}{Q_i}(Q_i - \dot{Q}) \tag{10}$$

where k is the strength of the force keeps the average distance between connected monomers stiffly constrained to relatively small fluctuations around $\dot{Q}$, separation distance in equilibrium state.

2.3.4. Intermolecular interaction

The intermolecular interaction represents the self-association between different monomers, which collapsed the VWF polymer into a relatively compact globule but

prevented any bead overlapping. A pairwise truncated Lennard-Jones interaction force is used to model this interaction,

$$
\mathbf{F}_{ij}^{In} = -k_B T
\begin{cases}
\dfrac{4\varepsilon}{d^{ev}}\left[12\left(\dfrac{d^{ev}}{r_{ij}}\right)^{13} - 6\left(\dfrac{d^{ev}}{r_{ij}}\right)^{7}\right]\hat{\mathbf{r}}_{ij}\,, & r_{ij} \geq 3 \\[4mm]
\dfrac{4\varepsilon}{d^{ev}}\left[12\left(\dfrac{d^{ev}}{3}\right)^{13} - 6\left(\dfrac{d^{ev}}{3}\right)^{7}\right]\hat{\mathbf{r}}_{ij}\,, & r_{ij} < 3
\end{cases}
\tag{11}
$$

where $\hat{\mathbf{r}}_{ij}$ is the unit vector along $\mathbf{r}_{ij}$, $r_{ij} \equiv |\mathbf{r}_{ij}|$, and ε and d^{ev} are the energy and length parameters, respectively. A constant repulsive force below a reduced distance of 3 acts to prevent bead overlapping while maintaining numerical stability during simulations; the value of 3 is slightly smaller than a bead diameter is chosen to produce the same level of maximum repulsive force as Larson et al. (56)

2.3.5. Brownian motion

The Brownian force is a random force which fluctuates rapidly due to thermal bombardment of the polymer by solvent. According to fluctuation-dissipation theorem, over a long time scale, the average of the random force should tend to zero; a relationship must exist between Brownian motion and drag, since the rate of Brownian motion reflects the diffusion coefficient, which is related to the drag coefficient. (45) A general form of fluctuation-dissipation theorem in the absence of HI is given by (57),

$$
\begin{aligned}
\langle \boldsymbol{F}_i^B(t)\rangle &= 0 \\
\langle \boldsymbol{F}_i^B(t)\boldsymbol{F}_i^B(t')\rangle &= 2k_B T\zeta\delta(t - t')
\end{aligned}
\tag{12}
$$

where $\delta(t-t')$ is the Dirac delta function. Thus, the Brownian force averaged over a time scale Δt becomes

$$
\boldsymbol{F}_i^B = \left(\frac{6k_B T\zeta}{\Delta t}\right)^{1/2}\boldsymbol{n},
\tag{13}
$$

23

where n is a random three-dimensional vector, each component of which is uniformly distributed in the interval [-1, 1]. (57) Considering the inverse of the average of the square of the 3-dimensional random vector, an additional factor 3 along with the factor of 2 from Eq. (12) gives the factor of 6 in Eq. (13). (45) To include HI, the fluctuation-dissipation theorem has a square root relationship between $\mathbf{D}_{ij}$ and $\boldsymbol{\sigma}_{ij}$

$$\mathbf{D}_{ij} = \sum_{l=1} \boldsymbol{\sigma}_{il} \cdot \boldsymbol{\sigma}_{jl}. \tag{14}$$

Here, both $\mathbf{D}_{ij}$ and $\boldsymbol{\sigma}_{ij}$ are second-order tensors (i.e. 3×3), while the overall tensor $\mathbf{D}$ and $\boldsymbol{\sigma}$ are fourth-order tensors(i.e. $3N \times 3N$). The calculation of $\boldsymbol{\sigma}$ is obtained by performing Cholesky decomposition. By including HI, the Brownian force is given by

$$\boldsymbol{F}_i^B = (\frac{6k_B T\zeta}{\Delta t})^{1/2} \sum_{j=1}^{n} \boldsymbol{\sigma}_{ij} \cdot \boldsymbol{n} \tag{15}$$

2.3.5. Boundary effect

To simulate VWF multimer binds to collagen exposed from injured blood vessel wall, it is necessary to keep VWF multimer entities (i.e. beads) near but not crossing the planar surface. Here, the lower boundary is obtained by applying a force term with Heaviside function is used (31)

$$\boldsymbol{F}_i^{LW} = k_B T \left[\frac{3a}{z_i-a} - \frac{3}{2a}\right] \Theta(3a - z_i)\hat{\mathbf{z}} \tag{16}$$

where a is the radius of beads, $\hat{\mathbf{z}}$ is the unit vector in the direction normal to the wall and z_i is the distance between the center-of-mass of a bead and the lower wall. Note that collagen binding sites are placed uniformly at $z = 3a$. Once a bead has a lower position than the collagen binding sites, the wall starts to exert a repulsive force that pushes the bead

away from the way. The higher boundary is performed by a $F_i^{HW} = -\frac{0.7k_BT}{\tilde{z}_i}\hat{z}$, where $\tilde{z}_i$ is

the distance between a bead and the higher wall. Thus, the total force due to boundaries is

given by

$$F_i^W = F_i^{LW} + F_i^{HW} = k_BT\left[\left(\frac{3a}{z_i - a} - \frac{3}{2a}\right)\Theta(3a - z_i) - \frac{0.7}{\tilde{z}_i}\right]\hat{z} \tag{17}$$

The boundaries only exist when study the A3 domain - collagen interaction. Simulations

of polymer chains in other studies do not have any spatial constraints.

2.3.6. A3 domain collagen binding force

When a bond is formed between an A3 domain in VWF and a collagen binding site,

the bond force is simulated by F_i^C and expresses as a harmonic spring

$$F_i^C = \tilde{k}Q_i w_{i,j,t} \tag{18}$$

where $\tilde{k}$ is the strength of the force and Q_i is the vector from the binding site to the position

of bead i. $w_{i,j,t}$ is a time-evolution matrix accounting for the status of the binding between

monomer i and a surface binder j at time t, with 1 indicating that there is binding and 0

indicating the absence of a binding interaction. The evolution of the matrix, $w_{i,j,t}$, is

governed by

$$w_{i,j,t} = \begin{cases} \begin{cases} 1 \; if \; \Xi < e^{-\Delta\tilde{E}_B} \\ 0 \; if \; \Xi > e^{-\Delta\tilde{E}_B} \end{cases} & if \; w_{i,j,t-1} = 0 \; and \; q_i \leq \tilde{q} \\ \begin{cases} 0 \; if \; \Xi < e^{-\Delta\tilde{E}_{UB}+\dot{f}\Delta x} \\ 1 \; if \; \Xi > e^{-\Delta\tilde{E}_{UB}+\dot{f}\Delta x} \end{cases} & if \; w_{i,j,t-1} = 1 \end{cases} \tag{19}$$

25

The state of $w_{i,j,t}$ depends on the binding transition probabilities $e^{-\Delta \tilde{E}_B}$ and $e^{-\Delta \tilde{E}_{UB}}$, the previous state $w_{i,j,t-1}$, and reaction radius $\tilde{q}$ within which the reaction may occur. $\Delta \tilde{E}_B$ and $\Delta \tilde{E}_{UB}$ represent the activation energies of binding and unbinding, respectively. Ξ is a randomly generated number between 0 and 1. $\dot{f}$ is the component of the external force on the bound bead that lies along the bead-binding site direction and $\dot{r}$ is the spatial distance from the minimum of the bound potential well to the energy barrier along the reaction coordinate, $\Delta x = 0\ nm$ represents suppressed slip bind, also refers to no-slip bond. Nonetheless, details of Δx for slip bond are discussed further in the Parameterization section below. Only one bead in each VWF monomer was permitted to bind to collagen binding sites in order to model the presence of the A3 domain in a certain region of the monomer. Furthermore, each collagen binding site could only bind to a single model A3 domain at any given time.

2.4. Parameterization of von Willebrand Factor Model

2.4.1. Parameterization

Parameters used in the model described above were obtained by optimizing against experimental data, where available. For parameters in the FENE spring, data from Ref. (37) were used to compute $H = 0.1428\ mN/m$ and $Q_0 = 60\ nm$. As presented previously, these two values were obtained by performing a curve-fit to the A2 domain force-extension data using the FENE spring law. (37, 46) In the simulations, the bead radius $a = 10\ nm$, which is half of the experimentally observed length of the fully unfolded monomer (80 nm) minus the maximum extended length for the FENE spring Q_0. The length parameter in the Lennard-Jones potential $\sigma = 20/2^{1/6}\ nm$ is approximately two times the bead

26

radius. To model the VWF multimer as being in a poor solvent, it should be in a globule state at zero and low flow regimes. This was achieved with an energy parameter in the Lennard-Jones interaction $\varepsilon = 0.52 k_b T$ (58) and length parameter $d^{ev} = 17.81\ nm$. For harmonic springs, $\dot{Q} = 21.54\ nm$, which is slightly larger than two times the bead radius, determined from considerations of VWF monomer-monomer separation distance.

Single-molecule pulling experiments were conducted to elucidate VWF-collagen interactions and results were used to parameterize the Bell model for describing unbinding of a VWF monomer from collagen. As discussed further in Results and Discussion, the experimentally obtained activation energy for unbinding was $\Delta E_{UB} = 5.7 \pm 0.7\ kT$. For results presented here, $\Delta E_{UB} = 6\ kT$ was used throughout; furthermore, to examine our model at an energy range similar to that focused on in Ref. (31), $\Delta E_0 = -2\ kT$ such that $\Delta E_B = 4\ kT$. Recall from above that experimental evidence exists suggesting $\Delta E_0 < -2\ kT$; in the Results and Discussion section below, how such a change to the model might affect data obtained is presented. Reaction radius $\tilde{q} = 10\ m$. For calculations presented here, the distance between collagen binding sites uniformly distributed in a square grid on the surface was $43\ nm$. Temperature is fixed at $T = 300\ K$ for all simulations. Table 2.1 below listed all the parameters that used in this study.

Parameter	Symbol	Value
FENE Spring Constant	H	$0.1428\ pN/nm$
Harmonic Spring Constant	k	$100\ k_bT$
Maximum Extendable Length for Harmonic Springs	$\dot{Q}$	$21.54\ nm$
Maximum Extendable Length for FENE Springs	Q_0	$60\ nm$
Bead Radius	a	$10\ nm$
Lennard-Jones Energy Parameter	ε	$0.52\ k_bT$
Lennard-Jones Length Parameter	d^{ev}	$17.81\ nm$
Temperature	T	$300K$
Viscosity	μ	$0.001\ pN\cdot\mu s/nm^2$
Drag Coefficient	$\zeta = 6\pi\eta a$	$0.1885\ pN\cdot\mu s/nm$
Collagen binding strength	$\tilde{k}$	$100\ k_bT$
Activating energy of binding	ΔE_B	$4\ k_bT$
Activating energy of unbinding	ΔE_{UB}	$6\ k_bT$
Reaction radius	$\tilde{q}$	$10\ nm$

Table 1 List of parameters.

2.4.2. Non-dimensional procedure

Variables in this work were made dimensionless by scaling length with $\sqrt{k_b T/H}$, force with $\sqrt{Hk_b T}$, and time with ζ/H, where H is the spring constant in the FENE spring term and ζ is the drag coefficient defined as $\zeta = 6\pi\eta a$ with η denotes the viscosity of the fluid. The energy parameters used in the forces are made dimensionless by $k_b T$. The dimensionless form of parameters is in Table 2.2 below.

Parameter	Dimensional Form	Dimensionless Form
Length	$\sqrt{k_b T/H} = 5.3846\ nm$	1
Force	$\sqrt{Hk_b T} = 0.7692\ pN$	1
time	$\zeta/H = 1.319\ \mu s$	1
Energy	$k_b T$	1
k	$100\ k_b T$	100
$\dot{Q}$	$21.54\ nm$	4
Q_0	$60\ nm$	11.14
a	$10\ nm$	1.857
ε	$0.52\ k_b T$	0.52
d^{ev}	$17.81\ nm$	3.3088
$\tilde{k}$	$100\ k_b T$	100
ΔE_B	$4\ k_b T$	4
ΔE_{UB}	$6\ k_b T$	6
$\tilde{q}$	$10\ nm$	1.857

Table 2 Comparison of parameters between dimensional and dimensionless form.

3. Simulation Techniques

3.1. Governing equation

By substituting Hi into Eq. (2), the stochastic differential equation including HI becomes

$$\dot{\mathbf{r}}_i = (\nabla \mathbf{u})^T \cdot \mathbf{r}_i + \sum_{j=1}^{N} \boldsymbol{\nabla}_j \cdot \mathbf{D}_{ij} + \sum_{j=1}^{N} \frac{\mathbf{D}_{ij} \cdot \left(\mathbf{F}_j^S + \mathbf{F}_j^{In} + \mathbf{F}_j^B \right)}{k_B T}. \tag{20}$$

The second term, $\boldsymbol{\nabla}_j \cdot \mathbf{D}_{ij}$ compensates for the spurious flus due to inhomogeneities in the diffusion tensor, which is identically zero in the cases where $\mathbf{D}$ is taken to be OB or RPY tensors. However, with the presence of boundaries, this term is nonzero, and computed as

$$\boldsymbol{\nabla}_j \cdot \mathbf{D}_{ij} = \left(\frac{1.125a}{z_i^2} - \frac{1.5a^3}{z_i^4} \right) \hat{\mathbf{z}} \tag{21}$$

By incorporating the forces and applying dimensionless scales, the discretized Langevin equation for bead i is given by

$$\mathbf{r}_i = \mathbf{r}_i^{old} + \left[(\nabla \boldsymbol{u})^T \cdot \mathbf{r}_i + \sum_{j=1}^{N} \boldsymbol{D}_{ij} \left(\boldsymbol{F}_j^S - \boldsymbol{F}_{j-1}^S + \boldsymbol{F}_j^{In} + \boldsymbol{F}_j^W + \boldsymbol{F}_j^C \right) + \sum_{j=1}^{N} \boldsymbol{\nabla}_j \cdot \boldsymbol{D}_{ij} \right] \Delta t +$$

$$\sqrt{6\Delta t} \sum_{j=1}^{i} \boldsymbol{\sigma}_{ij} \, \boldsymbol{n}_j \tag{22}$$

where $\mathbf{r}_i$ and $\mathbf{r}_i^{old}$ are the position vectors of bead i at the new and old times respectively.

3.2. Simulation details

Simulations were conducted to characterize the behavior of VWF multimers for 100 times longer than their computed longest relaxation time. (Chosen of longest relaxation time will be discussed later in Chapter 3.) Simulations were conducted using the time-step $\Delta t = 10^{-5}$ in dimensionless time unit. The VWF multimers are modeled either in shear flow

or in elongational flow. For a pure shear flow, the velocity gradient of the flow field is given by

$$\nabla \mathbf{u} = \begin{pmatrix} 0 & 0 & \dot{\gamma} \\ 0 & 0 & 0 \\ 0 & 0 & 0 \end{pmatrix} \tag{23}$$

where $\dot{\gamma}$ is the shear rate. Under elongational flow, the velocity gradient is

$$\nabla \mathbf{u} = \begin{pmatrix} \dot{\varepsilon} & 0 & 0 \\ 0 & -\dot{\varepsilon}/2 & 0 \\ 0 & 0 & -\dot{\varepsilon}/2 \end{pmatrix} \tag{24}$$

where $\dot{\varepsilon}$ is the shear rate. The Weissenberg number Wi is used to characterize the strength of flow. $Wi = \tau\dot{\gamma}$ (shear flow) or $Wi = \tau\dot{\varepsilon}$ (elongational flow), where τ is the longest relaxation time of VWF multimers. (46) The radius-of-gyration was computed to characterize the conformation of a VWF multimer and is defined as,

$$R_g = \sqrt{\frac{\langle \sum_{i=1}^{N} |\mathbf{r}_i - \mathbf{r}_{c,m}|^2 \rangle}{N}} \tag{25}$$

where $\mathbf{r}_i$ is the position of ith bead, $\mathbf{r}_{c,m}$ is the center of mass of the chain and $\langle \cdot \rangle$ denotes an ensemble average.

The initial conformation of each molecule modeled was generated by placing the first bead at 10 dimensionless units above the local origin. Subsequent beads were placed either 4 or 5 dimensionless units away from the preceding bead, depending on whether the two beads were connected by a harmonic or FENE spring, respectively. The actual position of placement was chosen randomly and 32 different initial conformations were used to improve ensemble averaging. The form of the bead-bead force expression is such that bead overlaps existing at time zero were quickly eliminated when the dynamic simulation began, while also maintaining numerical stability.

31

CHAPTER 3 *Flow-Induced Conformational Change of von Willebrand Factor*

1. Introduction

Significant research has been made in understanding flow-induced conformational changes in molecules such as VWF, some details of the process remain obscure. It remains unclear that how the dynamic conformation of a VWF multimer depends on details of its molecular architecture, including relative interaction strength between different domains in VWF. A motivation for understanding VWF is to potentially benefit the treatment of related diseases; another is the potential to synthesize molecules that mimic VWF behavior in some way. To achieve such goals, models would ideally possess the ability to make accurate quantitative predictions. While much has been gained from prior investigations based on coarse grain molecular models, it is important to advance new such models that directly incorporate into their description the growing body of experimental data from techniques such as single molecule force spectroscopy. This is further true for developing models of the interaction between different domains on VWF and relevant blood clotting species such as platelets and tissue walls. Since prior simulations have employed molecular models that did not attempt to incorporate submonomer mechanical properties observed in experiment, an opportunity exists to improve coarse grain molecular descriptions of flow sensitive biopolymers while maintaining relatively simple numerical implementation.

2. Simulation Details and Results

2.1. Molecular relaxation time

In all simulations in this dissertation, N is used to represent number of beads, thus the number of monomers is $N/2$. In order to compare simulation results of the vWF multimers with different length, the longest relaxation time τ has to be determined first. We compute τ by starting with a model of an extended vWF chain whose end-to-end distance is 70% of its contour length L. A collection of such chains was modeled in no-flow conditions until the VWF chains were fully relaxed to their equilibrium end-to-end distance values. The relaxation time was then computed by fitting the square of the end-to-end distance $\langle R^2 \rangle$ versus time t in the regime where statistical errors are relatively small. (56)

$$\langle R^2 \rangle - \langle R^2 \rangle_{eq} = A \, exp(-t/\tau) \qquad (26)$$

where $\langle R^2 \rangle_{eq}$ is the equilibrium value of $\langle R^2 \rangle$ and A is a constant. (59)

The relaxation curves for square of end-to-end distance versus time for one 60 beads VWF multimer are shown in Fig. 5. The longest relaxation time τ was measured in the regime where the ratio of end-to-end distance to L is less than 0.3. (59, 60) Obviously the 60 beads VWF multimer with HI is relaxing to a more globule-like state faster than without HI. Simulations with three different initial conformations have been done for same number of beads, which produced almost same results, meaning the initial conformation of VWF multimer has little influence on τ.

$<R^2>=36540 \exp(-t/615)+411$

$<R^2>=40340 \exp(-t/112)+2220$
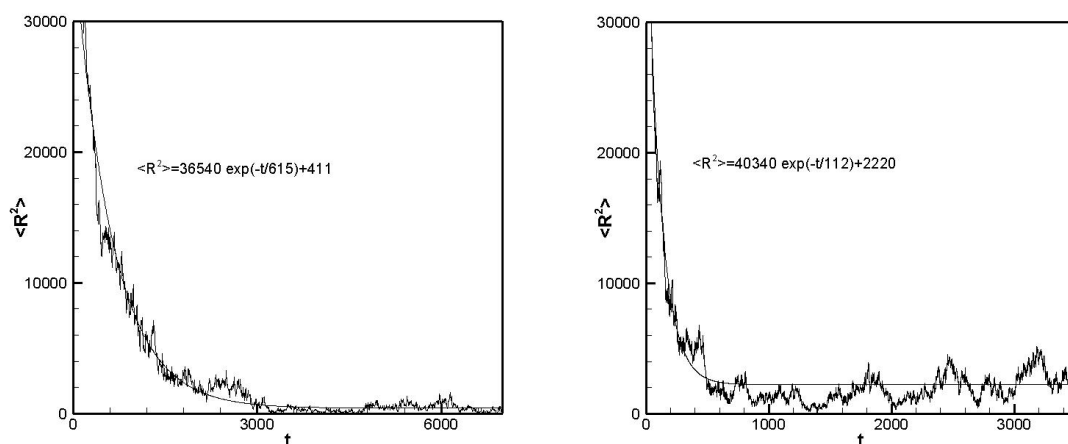
Figure 5 Relaxation curves for square of end to end distance versus time using 60 beads (A) without HI and (B) with HI.

The data in Fig. 6 is averaged over 32 VWF multimers with different random number starting seeds. Fig. 6 shows the longest relaxation time τ for different number of beads with and without HI. It also further shows that HI increases the rate of relaxation of VWF multimers to equilibrium from an extended state. Decreased relaxation time in the presence of HI is attributed to the so-called drag effect in that a preceding moving bead creates a stream pattern that pulls following beads in the direction of its motion. (51) It is found that a power-law scaling of relaxation time with number of beads exists, with exponents of 2.08 and 1.56 in simulations without and with HI. The R-squared values showing the quality of the fits are 0.99 for both FD and HI. In comparison, the Rouse relaxation time (without HI) and the Zimm relaxation time (with HI) depend on number of beads as $\tau_R \sim N^2$ and $\tau_Z \sim N^{3/2}$, respectively. (61)
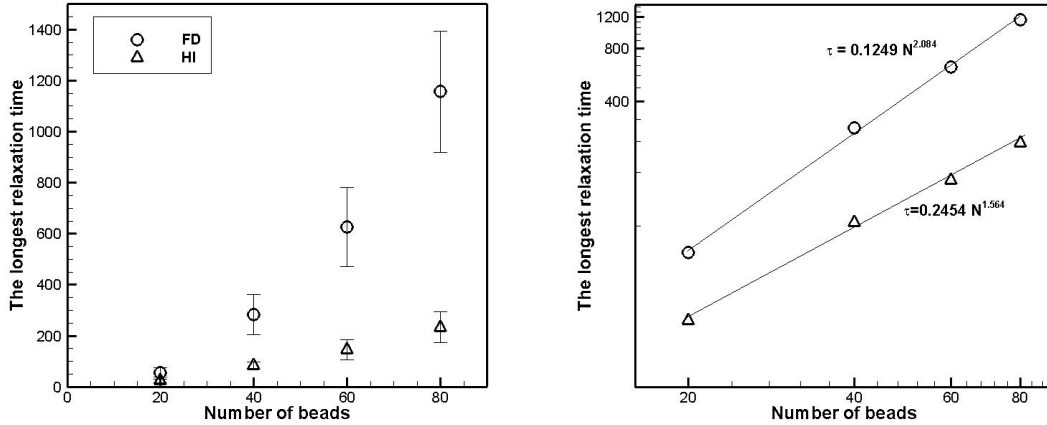
Figure 6 Dependence of the longest relaxation time τ on the number of beads N with and without hydrodynamics: (A) linear scale plot with error bar (confidence interval) and (B) log scale plot.

2.2. Molecular response in flow

In FD simulations, the HI effect is neglected. Fig. 7 shows the dependence of radius-of-gyration on the length of VWF multimer in a no-flow condition. We found that R_g scales as $N^{0.3197}$ that is close to the exponent of power law in poor solvent. Fig. 8 displays results during flow for the ensemble average of R_g normalized by $N^{0.3197}$ as a function of Wi. As expected, normalized R_g monotonically increases with Wi and then approaches an apparent asymptote, regardless of the length of the vWF multimer, which is the same behavior that Larson observed. (56, 62) Normalized R_g are approximately the same for all cases when Wi is below unity. The gap of the normalized R_g between different cases becomes more pronounced as Wi goes above unity, because longer vWF multimer has more potential to unfold and is more sensitive to flow conditions.

36
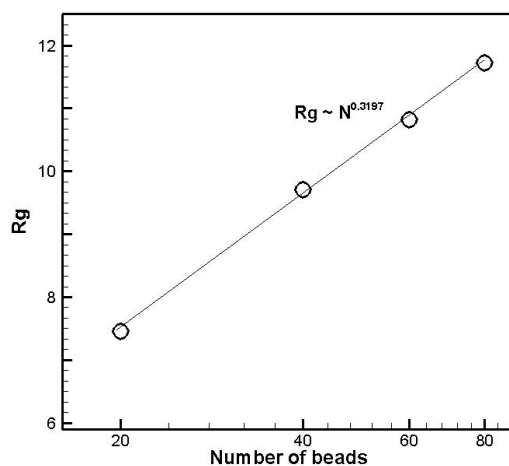
Figure 7 Dependence of the radius-of-gyration R_g on chain length N.
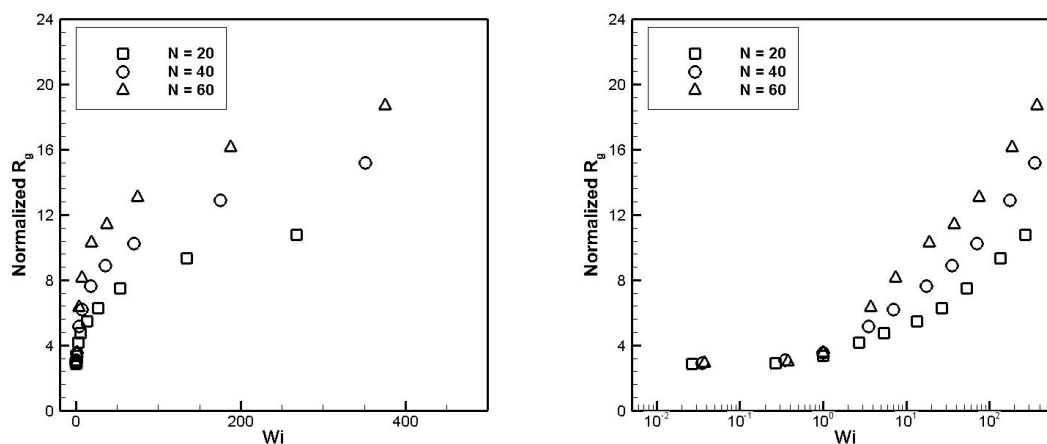
Figure 8 Dependence of the normalized radius-of-gyration R_g for different length of chains on Weissenberg number (Wi): (A) linear scale plot and (B) log scale plot.

Temporal characteristics for a single 60-bead VWF multimer under no flow condition and in $Wi = 1$ and 10 shear flow are represented in Fig. 9. As we see from $Wi = 10$ case, the vWF multimer reacted rapidly to the shear flow such that there is no apparent transient state. In that case, the ensemble average of R_g was calculated by averaging all data during a simulation run. For this specific 60-bead VWF multimer, the simulation running 100 times the longest relaxation time yielded ensemble average $R_g = 35.02$. As

we can see, the VWF multimer is significantly uncoiled at some points, which can enable the A3 domain to bind to collagen. Compared to $Wi = 10$ case, the vWF multimer exhibits fewer unfolding events and overall smaller fluctuations in $Wi = 1$ case, in which the assemble average $R_g = 13.04$. However, occasional significant degrees of unfolding of VWF multimers still occur at this relatively weak flow. This emphasizes the sensitivity of our model VWF molecules to shear flow. In no-flow conditions, the assemble average $R_g = 10.85$. Relatively little fluctuations persist in the no-flow case because the energy parameter is 1.43, which is strong enough to attract the beads to form a compact VWF globule.
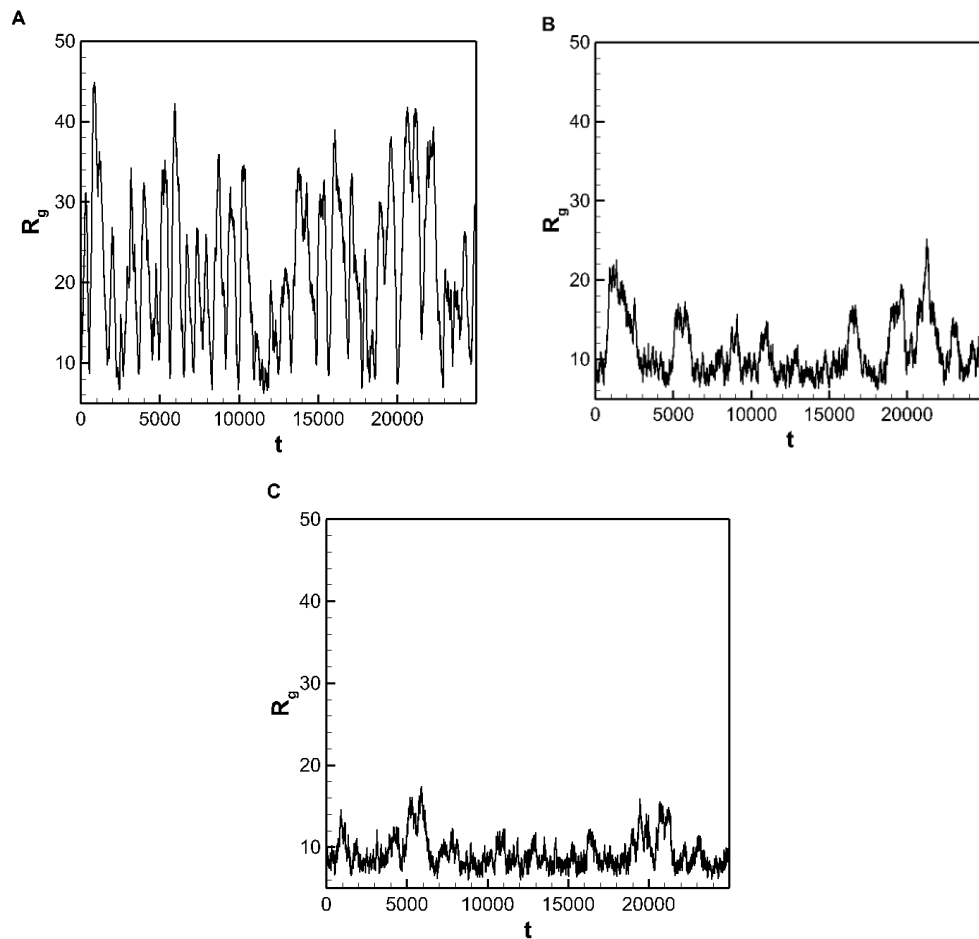
Figure 9 Time dependence for a 60-bead chain: (A) $Wi = 10$ case, (B) $Wi = 1$ case and (C) no flow case.

In hydrodynamic interaction simulations, the diffusion tensor for the RPY description **D** and weighting factor **σ** are solved at every time-step. The conformational behavior of 20-beads VWF multimers are tested under various strength of shear flow and compared with the results in FD. As seen in Fig. 10, HI has little effect on the conformational changes of VWF multimers when Wi is below unity. This is because the disturbance of the solvent by the slow motion of beads is negligible. When Wi is greater than unity, the rate of unfolding for HI cases is always smaller than for FD cases. The reason is that the beads hidden inside the protein are shielded from the flow and only a small fraction of the beads experience the fully drag force. A previously described shield effect predicting HI play a hindering role such that unfolding with HI requires a much stronger intensity of flow than without has been proved in our study. (51)

The critical Weissenberg number is around unity in Fig. 8 and 10, above which we observe a sharp transition of VWF multimer from a collapsed conformation to a stretched conformation. The critical shear rate to trigger the unfolding of VWF multimer measured by S.W. Schneider et al. in experiments is $\dot{\gamma}_{crit} = 5000 \ s^{-1}$. (32) After cleaved by ADAMTS 13, VWF multimers mostly have the length of 40 to 200 monomers. For a 80-beads VWF multimer (40 monomers), considering $Wi = 1$ is equivalent to a shear rate around $3500s^{-1}$ and the transition happens at $Wi > 1$, the critical shear rate for a 80-beads multimer predicted by our simulation results have a good agreement with the experiments.
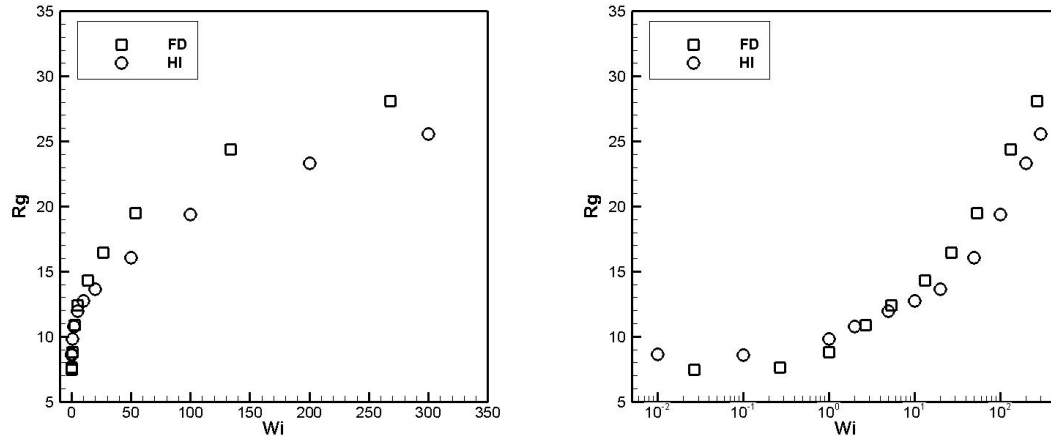
Figure 10 Dependence of the radius-of-gyration R_g for 20 beads vWF chains on Weissenberg number (Wi) for HI and FD cases: (A) linear scale plot and (B) log scale plot.

2.3. Intra-monomer domain response under flow

Results presented thus far underscore that the current model predicts multimer response to flow in very good agreement with prior simulations as well as available experimental data. A capability of the model presented is to simulate intra-monomer dynamics in terms of the elongational response of the FENE springs (i.e. the model A2 domains) to flow rate. Data in Fig. 11 show the ensemble average length of FENE springs in the FD case as a function of Wi as well as *N*. For $Wi < 10$, the model A2 domains remain at a length equal to that expressed at zero flow, which – in conjunction with adjacent beads – corresponds in real units to a monomer size near 40 nm. For $Wi > 10$, model A2 domain length increases with flow rate; at the highest Wi explored, the average value has nearly doubled or more, depending on *N*. Contrary to observations made from data in Fig. 8 for R_g versus Wi, data in Fig. 11 show that the dependence of the FENE spring length on Wi is stronger for smaller *N*. We explain this perhaps non-intuitive result in terms of data in Fig. 8. Larger molecules possess more modes of

40

dynamic structural response through which they interact with a flow field; therefore, larger molecules exhibit greater N dependence for molecular extension in high flow. Due to increased energy dissipation by molecular scale motion, less energy is dissipated by modes internal to the monomers. Thus, the dependence on Wi of the model A2 domain length is somewhat less for larger N.
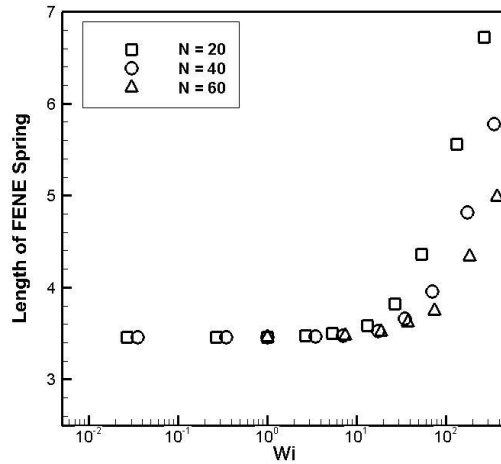
Figure 11 Dependence of the Length of FENE spring for different length of chains on Weissenberg number (*Wi*).

The model unfolding transition for the A2 domain occurs near $Wi = 10$ whereas, for this model and prior similar models, (28) multimer unfolding occurs for flow greater than $Wi = 1$. This order of magnitude increase for intra-monomer domain unfolding is likely reflective of a smaller relaxation time for FENE springs compared to the relaxation time for the multimer; the latter was the value used in computing Wi in Fig. 11. We did not attempt to compute a relaxation time for the FENE spring alone; however, supporting evidence for a significantly lower relaxation time is discussed below in regard to fluctuation dynamics for FENE springs in high flow. The overarching conclusion is that,

41

as flow increases, the current model predicts a molecular unfolding transition that emerges at lower flow rate than a sub-monomer domain unfolding transition at higher flow rate.

Similar to data shown in Fig. 9 for the time dependence of R_g at multiple flow rates, Fig. 12 shows analogous data for the FENE chain length time dependence. In this case, data are only shown for zero flow and $Wi = 100$ and, for the latter, significant fluctuations are manifest in the model A2 domain dynamics. Indeed, there are periodic excursions where the model A2 domain becomes nearly completely unfolded. As mentioned above, the fluctuation period observed in Fig. 12 is significantly smaller than that observed in Fig. 9; this supports the notion that FENE springs exhibit a significantly lower relaxation time than multimers. In accord with the model domain unfolding transition occurring near $Wi = 10$, significant fluctuations in the FENE spring dynamics do not emerge until above this transition as well. Data are only shown for $N = 20$; however, this analysis was done for all cases studied. Similar to the average FENE spring data, fluctuations in FENE spring length decrease somewhat with increasing N. However, this effect is small and all cases studied exhibited periodic excursions to nearly complete unfolding of the model A2 domain in high flow scenarios. The effect of HI on intra-monomer dynamics was explored for $N = 20$ and it was found for that case that the inclusion of HI had negligible effects on intra-monomer dynamics. It remains possible that HI may have greater effect on the behavior of the model A2 domains for larger N and this will be a focus of future work.
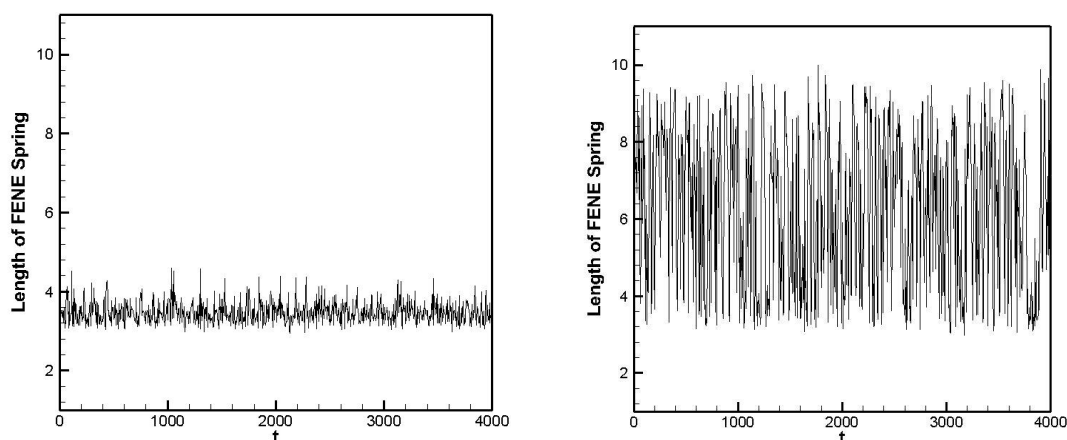
Figure 12 Time dependence of the length of FENE spring for a 20-bead chain: (A) *Wi* = 0 case, (B) *Wi* = 100 case.

Results here demonstrate the power of the current model in revealing not only multimer response to flow, but also intra-monomer domain response to flow. One role of the A2 domain is to interact with the ADAMTS13 enzyme to achieve scission of, in particular, ultra large VWF multimers in blood. The site in the A2 domain at which proteolysis occurs is shielded from the enzyme when multimers are in a compact globule conformation. For all cases studied here, the model A2 domains exhibit periodic complete unfolding at high flow rate; such behavior would abet interaction with ADAMTS13, leading to scission. Though larger N here was seen to result in a smaller dependence of the model A2 domain extension on flow, the dependence on N was relatively small. This was particularly true with regard to fluctuations. Furthermore, larger N means that a larger number of A2 domains are undergoing observed periodic complete expansion. Thus, for larger N, the likelihood for interaction between the A2 domain and ADAMTS13 is higher because more A2 domains are being exposed. More detailed of As domains length response to flow is discussed further in Chapter 5.

3. Conclusion

In this chapter, a realistic VWF model has been proposed that exploits experimental observations that A2 domains of VWF monomers have low resistance to unfolding. Given this, the A2 domain in the presented model is treated as a FENE spring with significant extensibility. The rigid domains of each VWF monomer are treated as two beads attached to one another by the FENE spring. Adjacent monomers are connected by a tight harmonic spring between one bead on each monomer, thus forming VWF multimers. This model enabled us to capture some of the structural conformational changes, and corresponding mechanical response, inside each VWF monomer. The model is optimized by fitting parameters to experimentally observed data. The spring constant and the maximum extended length for the FENE spring are determined based on A2 domain force-extension experimental data. The energy and length parameters for Lennard-Jones potential are optimized to mimic coiled VWF globule in poor solvent without flow that the power law is $Rg \sim N^{1/3}$. Brownian dynamics simulations using this VWF model with the measured parameters have been performed to calculate the longest relaxation time τ of vWF multimer with different length in both FD and HI cases. The results revealed that the relaxation time with HI is much smaller than without HI for the same number of beads. A power-law scaling of relaxation time with number of beads exists, with exponents of 1.56 and 2.08 in simulations with and without HI. The same techniques have been used to study the conformational changes under various intensity of shear flow condition for a single VWF multimer. It is shown the length has a profound influence on characteristics of VWF multimer under flow. Longer VWF chain has been proven to have more potential to unfold.

The comparison of results with and without HI revealed that HI effect is critical for modeling flow-induced conformational changes of VWF multimer, which hinders unfolding of VWF multimer.

CHAPTER 4 *von Willebrand Factor Binding on collagen surface*

1. Introduction

As discussed earlier, VWF is a very large plasma protein that can be stretched by shear flow and extended to tens of microns. With such significant length, multimeric VWF carries many binding sites for platelets and collagen; Fig. 2 A shows a domain view of a VWF monomer and binding sites are believed to exist in multiple domains. One binding site, the A3 domain (shaded in Fig. 2 A), is located near the center of the monomer structure; this site exhibits strong binding with collagen. VWF biopolymers experience non-trivial hydrodynamic forces in the circulation system. It has been reported that VWF has force-sensing capability: the protein adopts a compact shape in normal circulatory status where shear rates range from tens to a few thousand per second; for shear rates greater than 5000 s^{-1}, VWF changes conformation to an elongated shape, increasing its interaction with platelets and collagen. Proper functioning of VWF is critical to human health; at least two human diseases are related to dysfunctional VWF. Type 2 von Willebrand Disease (VWD) is a commonly seen coagulation related condition that is caused by structurally abnormal multimeric VWF. Thrombotic thrombocytopenic purpura (TTP) is another hereditary blood disorder caused by VWF multimer abnormalities; symptoms include thrombus and blood clot formation throughout the body. (37, 63) Thus, great potential for benefit to the treatment of human disease can be had by developing better understanding of the mechanisms by which biopolymers like VWF adhere to relevant biological surfaces.

Though in a globule conformation at low shear, VWF is a very large plasma protein that can be extended to tens of microns. With such significant length, multimeric VWF carries many binding sites for platelets and collagen; Fig. 1 A shows a domain view of a VWF monomer and binding sites are believed to exist in multiple domains. One binding site, the A3 domain (shaded in Fig. 1 A), is located near the center of the monomer structure; this site exhibits strong binding with collagen, in particular collagen III (64), specifically via peptide 23. (65) VWF binding to platelets in blood is achieved via the A1 domain binding with the platelet glycoprotein Ibα. (66–68) Focus herein is on A3/collagen binding; nonetheless, it is interesting to note very recent evidence has been advanced that the A2 domain in VWF blocks the A1 domain in equilibrium conditions, thereby mediating A1/platelet binding. With sufficient shear forces, dissociation of A1 and A2 occurs – accompanied by partial A2 domain unfolding – to permit A1/platelet interaction. (69, 70)

It is counterintuitive that the wound healing process initiates by the adhesion of VWF multimers to exposed collagen. This implies that VWF multimers exhibit an increased potential for adhesion at high shear rate; however, theory and computational simulation using coarse grain molecular models have instead shown that many polymers detach from surfaces at high shear rate. (71) For example, Ma H. B developed a continuum theory and showed typical polymers migrate away from the wall in shear flow because of hydrodynamic interactions between the chains and the wall. A depletion layer formed near the wall, which was determined by the normal stresses that develop in flow. (72) R.R. Netz used Brownian hydrodynamic simulations and coarse grained molecular models to investigate polymer adsorption. He concluded that shear flow weakens the adsorption of flexible polymers by hydrodynamic lift. That work also identified surface friction as an

important factor because surface potential corrugation weakened surface attraction as well. (73) C.E. Sing found the hydrodynamic lift force displays a non-monotonic character, which increases linearly with the distance to the wall in near-surface regime and decays quadratically with the distance to the wall in far field. (74) Furthermore, S. Dutta et al. developed a kinetic theory incorporating monomer-wall (or bead-wall) hydrodynamic interactions to investigate adsorption of homopolymers to a planar wall. They concluded shear flow causes molecular migration, leading to desorption. Increase in the flow strength resulted in a decrease in the quantity adsorbed and the film thickness. (75, 76) R.R. Netz investigated adsorption behavior of collapsed homopolymers on different surface models. The surface models were distinguished into three types: homogenous adsorbing surface, homogenous surface with a stagnant boundary layer and inhomogeneous surface consisting of discrete binding sites. Globule adsorption for all three cases was not enhanced by the presence of shear. They concluded a more complex binding mechanism is needed to explain VWF adhesion behavior. (77) These studies clearly showed shear flow induced *desorption* of typical polymers; as such, they do not explain the observed shear-induced VWF adsorption process. One important distinction in the preceding discussion is between the use of adsorption versus binding; the modeling studies described above did not model bond-forming reactions between molecules and a surface; thus, when a molecule attached to a wall, it was due to a relatively weak interaction and therefore considered adsorbed. VWF reacts with collagen, forming a relatively strong chemical bond; thus, bond formation (binding) is crucial to the process.

More recently, some breakthroughs have been made that have further elucidated how VWF multimers adhere to a damaged vessel wall. Several interesting results

pertaining to VWF multimer adhesion in shear flow were revealed in experiments performed by Schneider et al. (32) Authors of that work found that, at quiescent state and low flow regimes, VWF multimer adhesion to a collagen coated surface was significantly reduced compared to what was observed at higher flow rates. More specifically, experimental data revealed that VWF multimers exhibit significant conformational unfolding at shear rate above $5{,}000 \ s^{-1}$ and that the conformational change is associated with a relatively sharp increase in the rate of adhesion. Based on the experimental facts that the unfolding and the adhesion of VWF multimers are concurrently happening, it was concluded that VWF multimer adhesion on a collagen-coated surface is triggered by its conformation. (32)

To investigate these experimental findings further, subsequent coarse-grain molecular simulation studies by Sing introduced Bell-model-type interactions to mimic bond formation between a VWF multimer and collagen. (31) Their simulations determined whether a bead in the molecular model (i.e. a monomer) became bound to the surface based on a proximity criterion between the bead position and a given binding site, as well as parameterized binding and unbinding energies. The underlying chemical notion is that an activated energy state E_{act} must be achieved to either bind with or unbind from a model collagen site; if the bound and unbound energy states are E_B and E_{UB}, respectively, then $\Delta E_B = E_{act} - E_{UB}$ and $\Delta E_{UB} = E_{act} - E_B$ are the energy barriers to bind and unbind, respectively. Furthermore, $\Delta E_0 = E_B - E_{UB} = \Delta E_B - \Delta E_{UB}$ is the net energy change that occurs upon binding. Such models also allow for an influence on the unbinding energy due to externally applied forces; in the limit that such effects are not included, bonds are called slip-resistant. (31) Authors of Ref. (31) focused on situations where $\Delta E_0 > \text{-}2 \ kT$,

where k is Boltzmann's constant and T is absolute temperature, and found that shear-induced adhesion only occurred if the VWF-collagen bonds in their model were slip-resistant; more significantly, authors of that work showed that a relatively large energy barrier to unbinding – or, equivalently, a long lifetime for bound states – was required. Based on their simulation results, the authors advanced a model of shear-induced adhesion that gives predictions in very good qualitative agreement with Schneider's experimental observations. (32) More recently, using a coarse-grain model similar to that used in Ref. (31) but a multi-particle collision dynamics approach for capturing solvent influence near a stationary wall, Heidari, et al., explored the role of molecule cooperativity in determining the likelihood for binding. (78) Those authors demonstrated that a previously bound VWF molecule induces an attractive force on a flowing VWF molecule, increasing its chance of moving toward collagen binding sites and becoming bound.

References (31) and (78) represent important steps toward using molecular scale models to understand VWF shear-induced binding. It is notable that both studies explored energy landscapes such that $\Delta E_0 > -2\,kT$; one explanation for this was to ensure that binding was relatively less probable in quiescent to low shear regimes. Specifically, in those articles, shear-induced binding was reported by showing the ensemble averaged fraction of time that a VWF molecule has more than one-fifth of its binding sites attached to collagen. Since a single binding site may be sufficient to anchor a VWF molecule, this selection seems dubious; however, this is not the case. The simulation methodology used in the previous simulation based studies (and also used herein) promotes binding even in cases where $\Delta E_0 = 0$. This is because prior work (and work here) utilizes a confining force field to keep molecules sufficiently close to binding sites during the simulations; this, in

combination with the nature of the Bell model and the number of binding sites per molecule ensures that the condition for binding will be periodically met with sufficient frequency. To suppress this completely, artificially large energy barriers are needed. While this highlights a limitation of the model, prior authors were still able to examine *relative* binding levels and demonstrate interesting trends that correlated well with experimental observations. Despite the simplicity of coarse-grain molecular models and the Bell binding model, Refs. (31) and (78) provided useful insight to shear-induced binding mechanisms of VWF.

Nonetheless, existing experimental observations lend evidence that VWF-collagen binding is stronger than $\Delta E_0 > -2 \, kT$ previously explored. For example, using surface plasmon based chemical techniques, binding between VWF and collagen was probed experimentally. (64, 65) It was initially found from obtained dissociation reaction rate constants that $\Delta E_0 \sim -20 \, kT$; in their later work, higher dissociation rate constants were obtained such that $\Delta E_0 \sim -13 \, kT$. Authors ascribed the larger values to the presence of multivalent VWF in the earlier samples and were thus likely overestimates for the single binding site ΔE_0. (65) While more work needs to be done exploring this energy landscape experimentally, the possibility of a stronger chemical affinity must be considered. It is also useful to consider what must be present in a coarse-grain molecular binding model to more significantly suppress binding at low shear; that is, if a molecule is considered bound once a single binding site has been established, then what is needed in models such as those presented in Refs. (31) and (78) to significantly suppress binding at low shear?

The VWF model employed here has been previously advanced in Chapter 2; it attempts to more realistically describe molecular architecture inherent in the protein by

modeling VWF monomers as a highly flexible A2 domain with relatively rigid domains on either side of A2. (46) In this chapter, we extend our previous research by studying adhesion of VWF multimers described by our model to a model collagen-coated surface. Collagen represents the majority of the total protein of the vessel wall and has been demonstrated to play a key role in binding with VWF. (64, 79, 80) Normally located under vascular endothelial cells, collagen binding sites are not exposed to blood flow. However, after injury, blood will flow over subendothelial structures including connective tissue that contains a high percentage of collagen. Then VWF multimers are able to bind to exposed collagen (and flowing platelets).

2. Numerical Model Details

2.1. Model description

A binding site to collagen in VWF monomers is located in the A3 domain. As such, in the model here, binding sites on model collagen surfaces can only interact with one bead (shaded in Fig. 2 B) of each VWF monomer. A3 domain and collagen interactions are represented by reversible ligand-receptor-type bonds based on Bell model kinetics. (31, 81–83) Surface corrugation is not considered in this study and bonds are modeled both in a no-slip limit, based on the findings in Ref (31).

Collagen binding sites are placed uniformly on the surface as shown in Fig. 13 as blue quadrilaterals with size neglected. Once a bead is within the reaction radius $\tilde{q}$, a Bell model will be adopted to determine if a bond is performed. The equilibrium length of the bond (if established) between model A3 domains and collagen binding site $\dot{q}$ is applied to

describe the separation distance between A3 domain and collagen binding sites. Similar to Sing et al (31), a lower boundary is $3a$, 5.57 dimensionless units, below the collagen binding sites, and holds a position at zero height ($z = 0$). The lower boundary constrains the polymer to the area above $z > 0$ by applying a potential when beads have a lower height than the collagen binding sites. The wall potential is chosen so that to be zero at $z = 3a$.
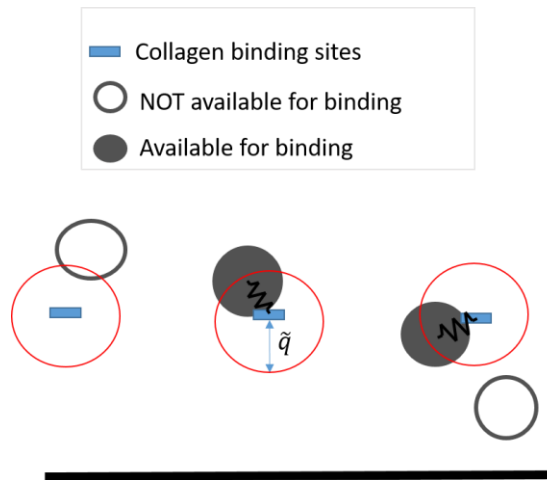
Figure 13 Schematic diagram of collagen binding sites distribution and reaction radius

In the prior work where the current authors presented the coarse-grain molecular model used here, data were presented for fluctuations of the model A2 domain length (i.e. the FENE spring length) as a function of time and at varying Wi. (46) Similar to what was observed for the overall molecular conformation, the average model A2 domain length and the fluctuation amplitude increased with increasing Wi, above some transition range. Thus, an additional criterion for binding was introduced for each eligible bead on a VWF chain: for a given bead to be able to bind to an open collagen binding site, in addition to the requirement that the bead be sufficiently close to the collagen binding site, it was

54

required that the model A2 domain (FENE spring) closest to the given bead be sufficiently elongated from the equilibrium extension of the FENE spring at zero flow conditions in bulk fluid. The justification/implications of this local, conformationally dependent condition are discussed below; the schematic in Fig. 14 illustrates this criterion. In both panels of Fig. 3, the bead is depicted to be sufficiently close to the binding site; in the panel on the left, the adjacent FENE spring is not sufficiently elongated so no random number is selected (i.e. according to the Bell model procedure) and the simulation proceeds. Thus, in the modified model, there exist three criteria for binding: a proximity requirement that the bead be within a reaction radius of an unbound collagen site, a length requirement that the A2 domain closest to the binding bead must be sufficiently elongated, and an energetic requirement that a randomly selected number between zero and one satisfy the conditions for binding as predicted by the Bell model. For unbinding, the length criterion is not applied and the proximity requirement is not meaningful. The order of tests for the criteria for binding were as presented (first proximity, then domain elongation, then energetic); this assumes a mechanism where the reaction cannot be sampled by a molecular entity until it adopts a certain conformational feature. Note that, at equilibrium, FENE springs in the model show finite extension; though it is small compared to the overall extensible length of the springs, it is reflective of the simplicity of representing the A2 domain with a FENE spring. A criterion for binding dependent upon model A2 domain extension can be normalized to either a percentage of the maximum extensible length or a percentage of the equilibrium length; here the latter is chosen and extension criteria between 20% and 30% were explored. If the former definition is used, these values would instead be between 1.8% and 2.7%.
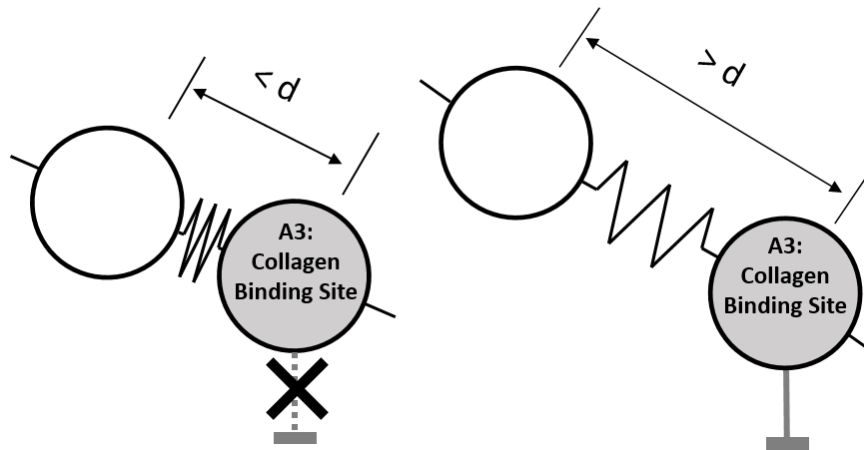
Figure 14 Schematic diagram of length criteria of A3 domain collagen binding

Figure 15 explains the details of binding check process. It is first required that the separation distance between an eligible bead (shaded) and collagen site satisfy the typical binding proximity requirement $\tilde{q}$ (criterion 1 in the right panel). Next, the model A2 domain (i.e. FENE spring) adjacent to the binding bead must be sufficiently elongated (i.e. that the spring length be greater than some parameter d). In the left schematic of criterion 2, the system is permitted to move to the next step; in the right schematic of criterion 2, the A2 domain elongation requirement is not met so binding is not allowed. Lastly, energy criterion is tested for binding to an eligible collagen site. In the text, the parameter $\tilde{q}$ is the reaction radius, d is expressed as a percentage elongation vary from 20% to 29%, relative to the equilibrium FENE elongation d_0 in our model. Ξ is a randomly generated number between 0 and 1.
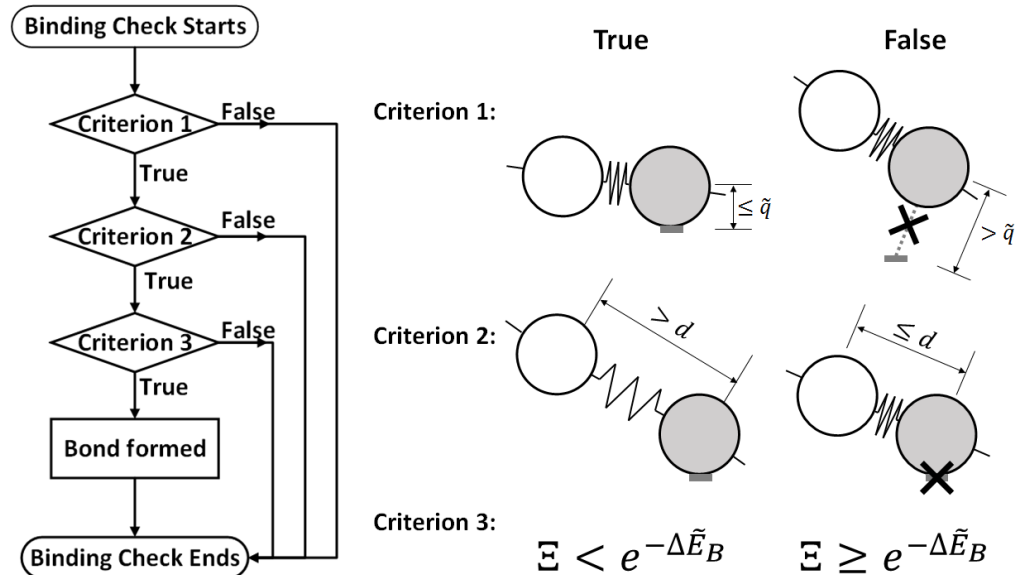
Figure 15 Schematic representation of the binding criteria. In the left panel, the flow chart explains how the binding check processed. Details of each criterion is listed in the right panel.

A top boundary which is a soft repulsive wall is used to constrain the polymer chain within a relevant volume. The top boundary is initialized at 10 reduced units above the highest bead, maintains the position for one longest relaxation time, and then gently move down. It reaches the final position at 15 reduced units above the lower boundary within four longest relaxation time.

Note that, besides the model described above, attempts have also been made with a different wall model. Unlike the current lower/upper boundaries, we applied only lower boundary with strong attraction to the polymer. Due to the attractive force applied, the polymers approached the binding sites near the boundary rapidly. However, such interaction had a huge effect on the conformation of the polymer, forcing the polymer near the surface, and restricting the movement in z direction. Hydrodynamic lift force was

limited even with large Wi. This model was found to be unsuitable for this study, thus we decided to adopt the lower/upper boundaries model.

2.2. Parameterization of von Willebrand Factor – Collagen adhesion

Where possible, model parameters were fit to reproduce experimentally observed data. The spring constant and the maximum extended length for the FENE spring were previously parameterized based on A2 domain force-extension experimental data. (37, 46) Reaction radius in the Bell model was $\tilde{q} = 18.85\ nm$ and the equilibrium length of the bond between model A3 domains and collagen binding sites $\dot{q} = 10\ nm$; the latter value was coarsely estimated from observations made in single molecule force-extension experiments. Prior authors have cautioned about introducing impulse forces when a reaction occurs between a binding bead and a surface collagen binding site that are separated by a distance greater than the equilibrium distance for the harmonic bond; such large tensile forces can influence the balance of binding/unbinding rates due to the presence of the slip (or catch) bond length parameter in the Bell model. (84) Methods exist to suppress such forces but they were not utilized here. As discussed above, focus here is on exploring the use of the conformation of a feature unique to our monomer model (i.e. the FENE spring as a model A2 domain) as a mechanism for abetting shear-induced binding between VWF and surface collagen sites. Focus is thus on no-slip bond conditions with only a small exploration of the influence of a slip-bond. For the slip-bond simulations performed, there was indeed an influence on unbinding rate observed when reaction sampling was performed every time step. When reaction sampling was performed every 10 or 100 time steps - for the small range of parameters explored here - impulse forces did

not influence this study's conclusions. Nonetheless future investigations of broader parameter ranges will consider this influence more closely. For calculations presented here, the distance between collagen binding sites uniformly distributed in a square grid on the surface was 40 nm.

2.3. Hydrodynamic interaction tensor near surface

As discussed in Chapter 2, the diffusivity tensor $\mathbf{D}$ is a fourth order tensor has a dimension of $N \times N$. Each component of $\mathbf{D}$ is a second order tensor by itself and has 3×3 components. The non-dimensional form of $\mathbf{D}_{ij}$ is given by

$$\mathbf{D}_{ij} = \delta_{ij}\mathbf{I} + \mathbf{\Omega}_{ij}. \tag{27}$$

When considering the boundary effect, Hoda *et al* (35) expressed $\mathbf{\Omega}_{ij}$ as

$$\mathbf{\Omega}_{ij} = \left(1 - \delta_{ij}\right)\mathbf{\Omega}^{\text{RPY}} + \mathbf{\Omega}^{\text{W}} \tag{28}$$

where $\mathbf{\Omega}^{\text{W}}$ is a correction term that associates with the no-slip condition at the surface. $\mathbf{\Omega}^{\text{W}}(\mathbf{r}_i, \mathbf{r}_j + \mathbf{a})$ relates velocity perturbation at position $\mathbf{r}_i$ to a point force at position $\mathbf{r}_j + \mathbf{a}$, which can be obtained by a Taylor series around $\mathbf{a} = 0$, where $\mathbf{a}$ is a radius vector connecting the center and a surface point of the bead. Thus, the HI between two beads can be obtained by Taylor expand $\mathbf{\Omega}^{\text{W}}(\mathbf{r}_i + \mathbf{a}, \mathbf{r}_j + \mathbf{a})$ around $\mathbf{a} = 0$. First three terms in the expansion leads to

$$\mathbf{\Omega}^{\text{W}}(\mathbf{r}_i, \mathbf{r}_j + \mathbf{a}) = \mathbf{\Omega}_{PF}^{W}(\mathbf{r}_i, \mathbf{r}_j) + \frac{2}{3}a^2\mathbf{\Omega}_{C}^{W}(\mathbf{r}_i, \mathbf{r}_j) \tag{29}$$

where Ω_{PF}^W is a point force and Ω_C^W accounts for the finite bead size. Blake et al (85) derived the Ω^W by using the method of images. The boundary HI effect between two beads is treated by a directly interaction between one bead and the image of the other bead,

$$\Omega_{PF}^W(\mathbf{r}_i, \mathbf{r}_j) = \frac{3a}{4}\left(-\mathbf{S}(\mathbf{r}_i - \mathbf{r}_j^{Im})\right) + 2z_0^2\mathbf{P}^D(\mathbf{r}_i - \mathbf{r}_j^{Im}) - 2z_0\mathbf{S}^D(\mathbf{r}_i - \mathbf{r}_j^{Im}) \quad (30)$$

where $\mathbf{r}_j^{Im}$ is the location of the image of bead j, z_0 is the perpendicular distance of the bead i from the wall, $\mathbf{S}$ is the free space Stokeslet, $\mathbf{P}^D$ is the potential dipole and $\mathbf{S}^D$ is the Stokeslet doublet. The tensor Ω_C^W is given by

$$\Omega_C^W = \frac{1}{2}\left(\Omega_{PD}^W(\mathbf{r}_i, \mathbf{r}_j) + \Omega_{PD}^W(\mathbf{r}_j, \mathbf{r}_i)^T\right) \quad (31)$$

where Ω_{PD}^W is a correction to the free space mobility tensor for a potential dipole to account for the no-slip condition at the surface.

3. Results and Discussion

3.1. von Willebrand Factor – Collagen binding under flow

In Fig. 15, results are presented for ensemble averaged binding probability versus Weissenberg number Wi; as the product of a natural molecular relaxation time (here, the elongational relaxation time) and the shear rate in the simulation, Wi is a dimensionless quantity effectively comparing the time scale of flow to the time scale for molecular response. It has been advanced previously with this model, as well as others, that a globule to elongated transition is observed for model VWF molecules above approximately $Wi =$

1. (46) This is in agreement with experiments, which have revealed a transition with shear

flow for VWF from a globule to elongated conformation and estimates give that this occurs

in the order of $Wi = 1$. Because binding of VWF to collagen is believed to be

conformationally dependent, it is expected (and was observed in Ref. (32)) that binding

only became pronounced after shear rate exceeded a value corresponding to the

globule/elongated transition. Thus, a model that reproduces this behavior should show low

binding probability at low shear rate; furthermore, probability should increase with rate

above some transition value or range of Wi. Note here that a molecule is considered bound

to the surface so long as a single site on the molecule is currently bound to a collagen site.

This definition is reasonable from a molecular motion point of view: in cases presented

here, bound molecules essentially halted their motion with flow in x; that is, they became

essentially anchored to the surface. This will be discussed further below.
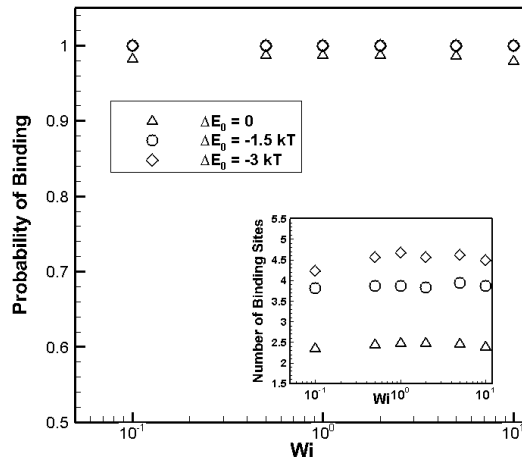
Figure 16 Binding probability for VWF molecules (10 monomers; 20 beads) as a function of Weissenberg number Wi. Data are presented for $\Delta E_0 = 0$ (triangles), $\Delta E_0 = -1.5\ kT$ (circles), and $\Delta E_0 = -3\ kT$ (diamonds). The inset shows (for the same values of ΔE_0) the ensemble average number of bonds between any molecule that is considered bound and the model collagen coated surface (at each timestep, a molecule is considered bound if at least one bond with the surface exists).

Results in Fig. 15 are for varying ΔE_0 and it can be seen that, for all cases considered, the model disagrees with experiment. For $\Delta E_0 < 0$, essentially every molecule is bound to collagen at all times; even for $\Delta E_0 = 0$, only a slight reduction in binding probability is observed. It was mentioned previously that results showed essentially no dependence on whether reaction sampling in the Bell model was done every 10 versus 100 steps. One notable difference was observed, but only for $\Delta E_0 = 0$: sampling every 100 steps showed a reduction in binding probability with Wi (from nearly 100% at zero flow to ~60% at $Wi = 10$). Given the well accepted result that hydrodynamic forces generate lift away from stationary surfaces, it is satisfying to see higher shear rate reduce binding probability and this could be an argument for sampling reactions less frequently (i.e. once every 100 steps). However, primary interest here is on cases where $\Delta E_0 < 0$ and, in those instances, no differences were observed between sampling once every 10 versus 100 steps. Thus, for figures here, data from simulations using a reaction sampling rate of one in every 10 steps are presented.

The inset to Fig. 15 shows the ensemble average of number of bonds between VWF molecules and the model collagen coated surface; there greater dependence on ΔE_0 is observed. Nonetheless, even for $\Delta E_0 = 0$, every molecule in the ensemble has, on average, 20% of its available binding sites actually bound to collagen. For $\Delta E_0 < 0$, this number is of order double, near 40%. For $\Delta E_0 = -3\ kT$, a small (but statistically significant) increase in number of binding sites is observed with increasing shear rate but this is subtle. This pronounced tendency for binding in the model used here (and in other related models) was discussed in the Introduction; because molecules are constrained to a simulation space near the binding sites, the nature of the Bell model (along with the energy

barriers, binding site density, and number of binding sites per molecule) ensures that a finite number of bonds will exist essentially at all times. This is why, in Refs. (31) and (78), binding probability was presented as an ensemble average of the number of molecules with more than 20% of their binding sites actually bound. However, as presented here, if a more absolute definition of bound is used, molecules are bound at essentially all time, particularly for $\Delta E_0 < 0$. Obviously, if a significantly larger ΔE_B is used, binding can be eliminated; however, observed reactivity of the VWF A3 domain with collagen does not warrant the use of such a high ΔE_B.

3.2. Length threshold of A2 domain in collagen binding simulation

In Fig. 16, binding probability versus Wi is again presented for varying ΔE_0; however, an elongation criterion of 23% was used for all simulations (again, this is 23% of the equilibrium extension of the FENE spring local, or adjacent to, a given binding bead). For $\Delta E_0 = 0$, binding is nearly eliminated completely at low shear flow (a small increase in binding is observed at the highest Wi explored). From this point in the discussion forward, we focus on situations where $\Delta E_0 < 0$, with special attention on $\Delta E_0 = -3\ kT$ since this is a binding energy for which prior authors predicted high affinity for binding even at low flow. We observed the same, of course, in the absence of any criterion on model A2 domain length. For cases where $\Delta E_0 < 0$ and extension criterion was 23%, binding at low flow is greatly reduced: for $\Delta E_0 = -1.5\ kT$, it is about 2% and, for $\Delta E_0 = -3\ kT$ it is just below 5%. Because a log scale is used, data for zero flow are not shown; however, they were - in all cases - a small percentage lower than values obtained for $Wi = 0.1$. The inset again shows the average number of bonds for bound molecules and it can

be seen that, in all cases except for $Wi > 2$, only a single bond exists. This provides some

indirect evidence to behavior observed in the simulation trajectories: at low flow,

molecules were - on average - mostly not bound and flowing in x. When a molecule

became bound, it was through a single connection that was subsequently broken to permit

the chain to continue to move with the flow. A notable observation in Fig. 16, for cases

where $\Delta E_0 < 0$, is a non-linear increase in binding for $Wi > 5$ ($\Delta E_0 = -1.5\ kT$) or for

$Wi > 2$ ($\Delta E_0 = -3\ kT$). For $\Delta E_0 = -3\ kT$, at the highest shear rate explored, binding

probability is over 20% and the number of binding sites begins to exhibit increasing

behavior. For $\Delta E_0 = -1.5\ kT$, the magnitude of probability is less but the increase with

shear rate is nonetheless notable.
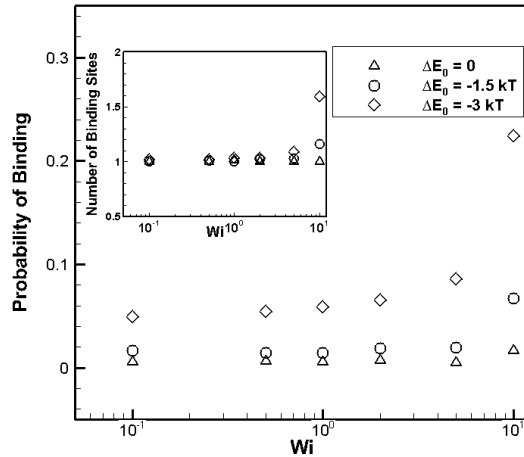
Figure 17 Binding probability versus Wi using the same symbol designation as in Fig. 2; for all cases of ΔE_0 illustrated, the A2 domain elongation criterion was set to 23%. The inset shows number of bonds per bound molecule as a function of Wi.

Data in Fig. 17 bear out that, for $\Delta E_0 = -3\ kT$, binding probability increases by a

factor of between four and five from low shear rate to high; furthermore, the dependence

of probability on shear rate below a transition region is much less pronounced than after

the transition. Given this satisfying agreement with experimental observations, further investigations only use $\Delta E_0 = -3\,kT$. For that case, Fig. 17 shows the effect of varying the length criterion between approximately 20% and 30%. The qualitative behavior described in Fig. 4 for $\Delta E_0 = -3\,kT$ persists for all length criteria shown in Fig. 17. For the two highest length criteria explored (26% and 29%), binding at low flow is essentially the same (~2% probability for binding). For both of those elongation criteria, binding probability again appears to transition to a greater dependence on shear rate for $Wi > 2$. Lastly for both those cases, the maximum observed binding probability is of order five to seven times what was observed at zero flow. For all length criteria explored, a notable correlation was observed between length criterion and maximum difference in binding probability (i.e. between low and high shear rate). Also for all length criteria, the average number of binding sites increases but, in all cases, this average remains below 2.
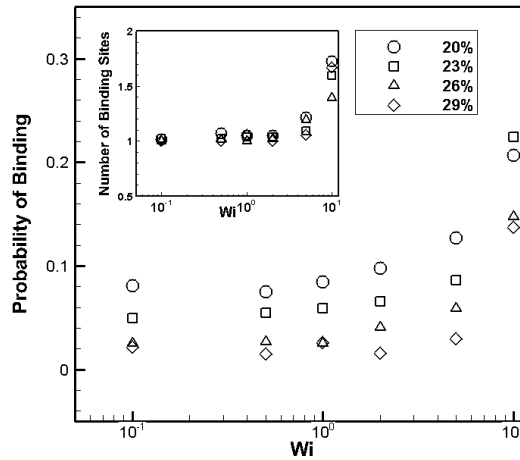
Figure 18 Binding probability versus Wi; for all data shown, $\Delta E_0 = -3\,kT$. The influence of varying the A2 domain elongation criterion is examined; data are for elongation criteria 20% (circles), 23% (squares), 26% (triangles), and 29% (diamonds). The inset shows number of bonds per bound molecule as a function of Wi.

Perhaps not surprisingly, given the known behavior about the model A2 domain length with varying shear rate, the length criterion explored very effectively rectifies model predictions with experimental observations. At low flow, using the absolute definition that a single binding site is sufficient to label a molecule bound, this criterion significantly eliminates binding, despite molecules being constrained in z (i.e. near the binding sites) by the bounding force fields. Because the model A2 domain length exhibits a behavior analogous to what is exhibited by the entire molecule (i.e. a transition from globule, or unelongated, to elongated above a certain threshold range in shear rate), the length criterion for binding suppresses binding only before such a transition manifests. Thus, above this transition, binding probability starts to increase significantly with shear rate.

In a recent collection of papers, binding between the A1 domain in VWF and platelets in blood was explored experimentally; authors of those works presented very strong evidence supporting a mechanism for reaction where the A1 domain could only bind with a platelet if the adjacent A2 domain was sufficiently elongated. (same citations as in Intro) Though we are aware of no such similar study of reactivity between the A3 domain and collagen - more specifically, how reactivity relates to conformation of the adjacent A2 domain - this is essentially what our model modification represents. It is important to suggest any corresponding mechanism with great caution; the molecular model employed here is highly simplified, particularly when it comes to specific chemical activity of various domains. Nonetheless, results here suggest that it would be reasonable for such a mechanism to be revealed; furthermore, such a mechanism can explain shear-induced binding even for cases where binding energy ΔE_0 is significantly below zero (i.e. highly energetically favorable).

In the works exploring interactions between A1 domains and blood platelets (same as in Intro), it was pointed out that, though elongation of the A2 domain was required for reaction between the two, it was equally important that the A2 domain be not too greatly elongated. Related to this, herein, only a relatively small range in the length criterion was explored; this range was partly selected based on that same notion of constraining the model A2 domain total elongation in conditions explored. The reason behind this is that another role of VWF in the blood is that, once blood clotting has initiated, the species ADAMTS13 interacts with A2 domains to drive polymer scission at the A2 site. This is a way that VWF essentially turns off its activity after its initial job is complete. This is also how the size range of VWF in the blood is maintained in a proper functioning range: though they are typically secreted at much longer lengths than are considered functional, such long VWF molecules undergo A2 domain elongation transitions even in healthy blood flow conditions. This permits interaction with ADAMTS13 and concomitant scission of the VWF molecule to smaller functional fragments. Nonetheless, it may be relevant to consider a wider range of elongation criteria, particularly when other simulation parameters are varied, such as chain length.

Future work will consider varying chain length; however, it is not immediately obvious that changing that parameter will undo the primary conclusion here that a length criterion is successful at rectifying model predictions with experimental observations. It is necessary to understand if and how model parameters depend upon chain length (i.e. to achieve similar agreement with experiment); thus, parameter optimization remains an important future exercise. However, it was observed previously that the general behavior that, for shear rates below of order $Wi = 2$, model A2 domain length remains relatively

constrained near the equilibrium value and increases for higher flow. This bodes well that our model can be successfully applied to longer chain length. However, it should nonetheless be a subject of future study. For example, no dependence could be detected for preferential location of binding along the relatively short molecules explored here. For longer multimers, however, it has been asserted by prior studies that forces acting on sub-monomer structures, like the A2 domain, arising from hydrodynamics will increase with molecular length. Furthermore, the force exerted on a given sub-monomer structure also depends on where along the chain the monomer is located (with greater forces on more central monomers). Thus, longer chain length studies using the length criterion presented here should examine if preference manifests in where along a chain binding occurs. This could have non-trivial influence on the molecular conformation of bound molecules.

3.3. Slip – Bond of von Willebrand Factor- Collagen Binding

All results presented were for a no-slip bond condition (i.e. external force on a VWF-collagen bond has no influence on the unbinding energy ΔE_{UB}. Authors of Ref. (31) found that shear-induced adhesion only occurs in a no-slip bond limit. Here, for the only value of slip bond length parameter explored, none of the primary conclusions were changed. Generally, of course, a positive slip-bond length parameter in the model softens the unbinding energy barrier, thereby promoting the unbound state. Accordingly, for all cases explored with a finite length parameter in the Bell model, binding probabilities were reduced. In the absence of a length criterion for binding, however, the effect was negligible. For cases where length criteria for binding were used and binding probabilities were significantly less than one, slip bonds resulted in somewhat decreased binding probabilities. However, decreases were relatively consistent across results so the increase

in binding probability with increasing shear rate for $\Delta E_0 < 0$ cases was again observed. This feature of the model remains important and should perhaps garner greater attention in the future; however, relative to the operation of the length criterion that is the main focus here, it is of secondary nature.

4. Conclusion

A recently advanced coarse grain model for VWF multimers that includes a sub-monomer degree of freedom to represent an unfoldable domain in the monomer was used to study interaction of VWF with model collagen coated surfaces. A3 domain and collagen reactions were represented by reversible bonds based on Bell model kinetics. Here, a molecule is considered bound if any binding sites on the molecule are bonded to a collagen site (rather than a threshold percentage of sites as has been used in prior similar modeling studies). For the range of binding energy explored, Brownian dynamics simulations including hydrodynamic interactions showed nearly 100% binding probability with very little dependence on flow condition; this behavior is contrary to experimental observations for VWF. By introducing an additional criterion for binding that required the A2 domain (i.e. the FENE spring) adjacent to a binding bead to be sufficiently elongated for that bead to bind with a candidate collagen site, discrepancies with experiment were significantly reduced; that is, the model exhibits shear-induced binding in reasonable parameter ranges. A notable feature of this study is that a rectification for discrepancy with experiment was sought that exhibits shear-induced binding for situations in which the binding energy, or chemical strength, of the VWF-collagen bond is relatively large. The length criterion presented demonstrates such a property. The model A2 domain (i.e. the FENE spring) is

unique to our VWF monomer model; it is possible that a similar method could be used for models comprised of strictly harmonic bonds. It remains an important future investigation to understand the sensitivity of the presented method's success to the non-linear nature of the FENE spring force-extension behavior. All such studies using Bell model reaction methods will benefit tremendously from experiments exploring the energy landscape of VWF-collagen reactions. Our model predicts a conformational dependence in the mechanism for A3-collagen binding; probing this will require more detailed experimentation on VWF multimers that allows simultaneous evaluation of the reactivity with varying A2 elongation.

CHAPTER 5 *Single-molecule Force Spectroscopy Experiment*

1. Introduction

Mutations of VWF will cause VWD. Three main types of VWD have been found based on the clinical observation: Type 1 VWD, Type 2 VWD, and Type 3 VWD. Each of these three types has various subtypes. (2, 11, 12) Type 1 VWD is the most common form, representing about 75% of all cases. Type 1 VWD is usually caused by heterozygosity for the defective gene. In this type, the VWF works correctly, but the production is decreased. Next common type is Type 2 VWD, accounting for about 20% of all cases. In this type, the VWF is qualitatively defective which leads to abnormal platelet binding and multimerization. Amount all sub types of Type 2 VWD, Type 2A, decreased in platelet binding, represents about 15% of all VWD cases. Research shows that patients with Type 2A VWD have overly short VWF concatemers, and some type 2A mutations may cause abnormally force-dependent folding and unfolding. (2, 8, 86, 87) As mentioned in early chapters, A2 domain of VWF can be unfolded by elongational force, cleaved by ADAMTS13 and, by doing so, the size distribution of VWF reaches homeostasis. (8, 88) Mutations in A2 may lead to less unfolding time or prolong refolding time. In other words, these A2 mutants might stay unfolded or partially unfolded most of the time, making them easy to be recognized and cleaved by ADAMTS13. In this chapter, a Type 2A mutant, Mutant Q1541R, will be experimental studied. Mutant Q1541R is found in patients with Type 2A VWD, and the understanding of this mutant will help to understand the mechanism of defective A2 domain unfolding.

2. Experiment Setups

1.1. Platform – Miniature Optical Tweezers

The high gradient in the electric field occurring neat the waist of a tightly focused laser beam is associated with strong forces that can capture polarizable dielectric particles in three dimensions. (26, 89) The devices based on this effect enables optically trapping of small particles are better known as "optical traps" or "optical tweezers". Optical tweezers are widely used in biomaterials studies. (26, 89) The colloidal particles, picked by and moved around by a laser beam that refracted by a microscopic object, are usually attached to cells or single biomolecules. (90)
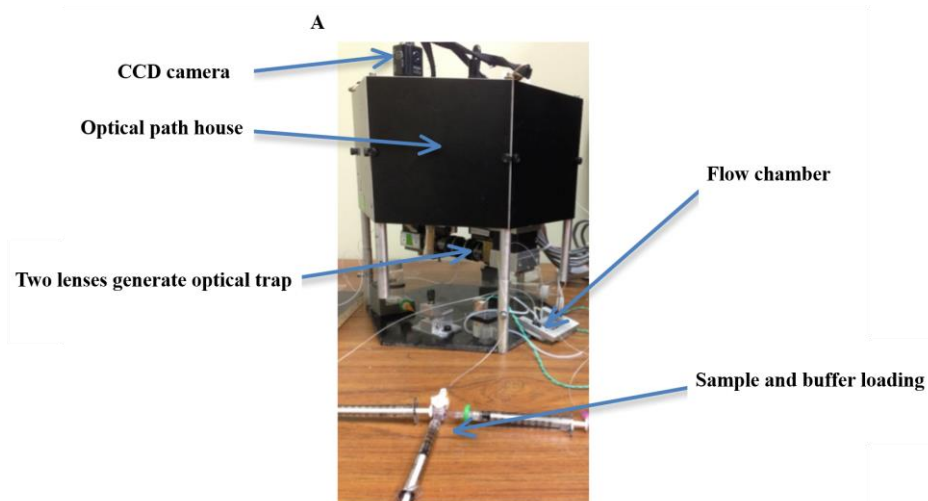
Figure 19 Optical tweezers.

The force exerted on the particles can be investigated by trapping the particles optically and moving the laser focus. From the perspective of biological application, optical

traps can achieve forces in sub-piconewton (10^{-12}) accuracy. The miniature optical tweezers shown in Fig. 19 directly measures force without complicated calibration steps or calculating force based on spring constants and displacements. Furthermore, better isolation from surrounding noises can be achieved because of its relatively small size, which gives the best reduction of the optical path length. By hanging up and isolating any possible variation or noise from operation desk, miniature optical tweezers can minimize the interference from surrounding and operator. However, the manipulation of the trapped particle can conduct force no larger than 100 piconewton (pN), which is not suitable for some single molecular experiments that require higher loading. AFM will be adopted for the cases require larger force loading but less accuracy. Fig. 20 shows the Fluidic setup of miniature optical tweezers.
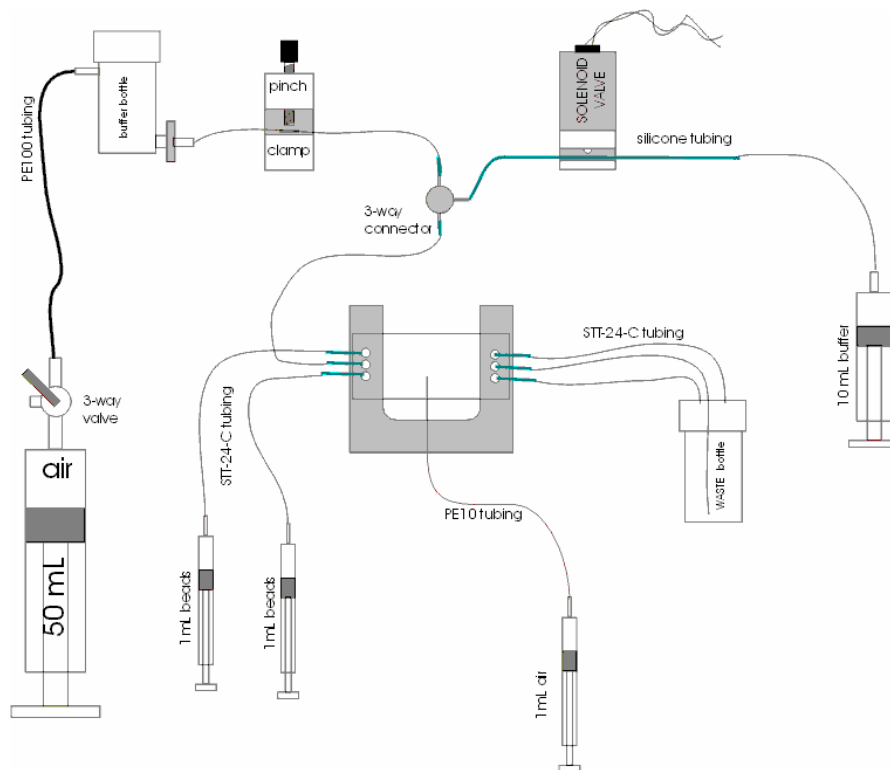
Figure 20 Fluidic setup of miniature optical tweezers. (Reprinted from http://tweezerslab.unipr.it/cgi-bin/mt/home.pl)

74

1.2. Materials and setup the pulling assay

Carboxyl-polystyrene 2.0 µm beads (10 mg, Spherotech, Lake Forest, IL) have been used in all the optical-tweezers experiments. Two gelatin free VWF antibodies are used in this chapter. Both of them are bought from Santa Cruz Biotechnology, Inc: the D'D3 monoclonal antibody (3E2D10) binds between amino acids 845 and 949 of the mature VWF and the C-terminus antibody (C-12) binds between amino acids 2779 and 2813 near the C-terminus of VWF. The antibodies are then treated with the Pierce™ Fab Preparation Kit (Thermo Scientific 44985) to generate the fragment antigen binding (Fab fragment) to strengthen the specification of the selected binding sites.

In this chapter, miniature optical tweezer is used to perform single molecular experiments on VWF mutant Q1541R. Both WT and Q1541R VWF multimer are provided by our collaborator Dr. Tom McKinnon from Imperial College London.

By holding the D'D3 domain and C-terminal of VWF mutant Q1541R multimer with SA beads, the A2 domain will unfold which allows observance of the Force vs. Extension properties for the mutant.

3. Results and Discussion

3.1 Unfolding assay on A2 domain of VWF

The laser trapped bead is moved to generate the approach and retraction curve while the other bead is fixed by the micropipette. For each approach, the trapped bead was driven to contact the fixed bead for 1 to 5 seconds to allow the A2 domain refolding

happens. The contact force is limited to be positive, which eliminates new tether to be performed but has neglectable effects on A2 domain refolding. A typical unfolding curve for VWF mutant 1541 multimer is shown in Fig 21.
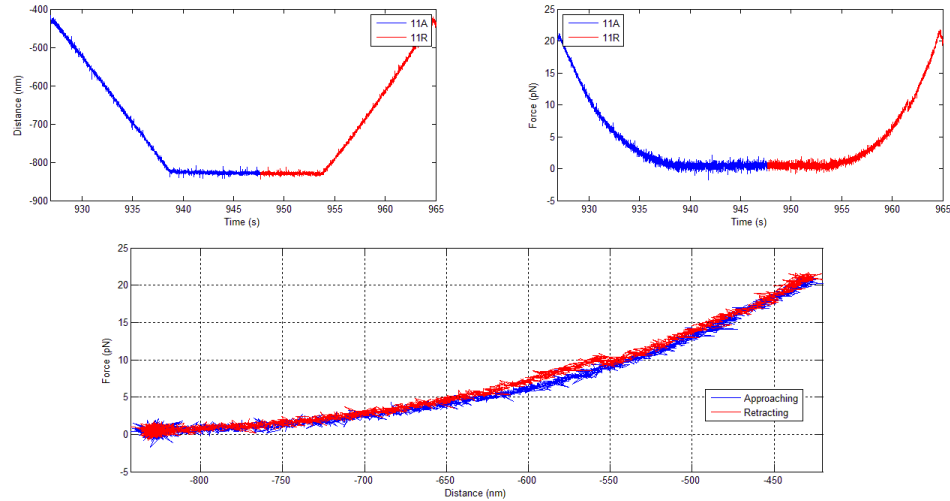
Figure 21 Typical unfolding curve of VWF A2 domain

3.2 Unfolding force vs extension of A2 domain of VWF

Various pulling speeds have been adopted to cover a wide range of unfolding behaviors: 50 nm/s, 100 nm/s, 150 nm/s, 200 nm/s, and 500 nm/s. Unfolding events are shown in Fig. 22 with different colors represents different pulling speeds. Most of the unfolding happens at 10 to 20 pN with 30 to 70 nm extension.
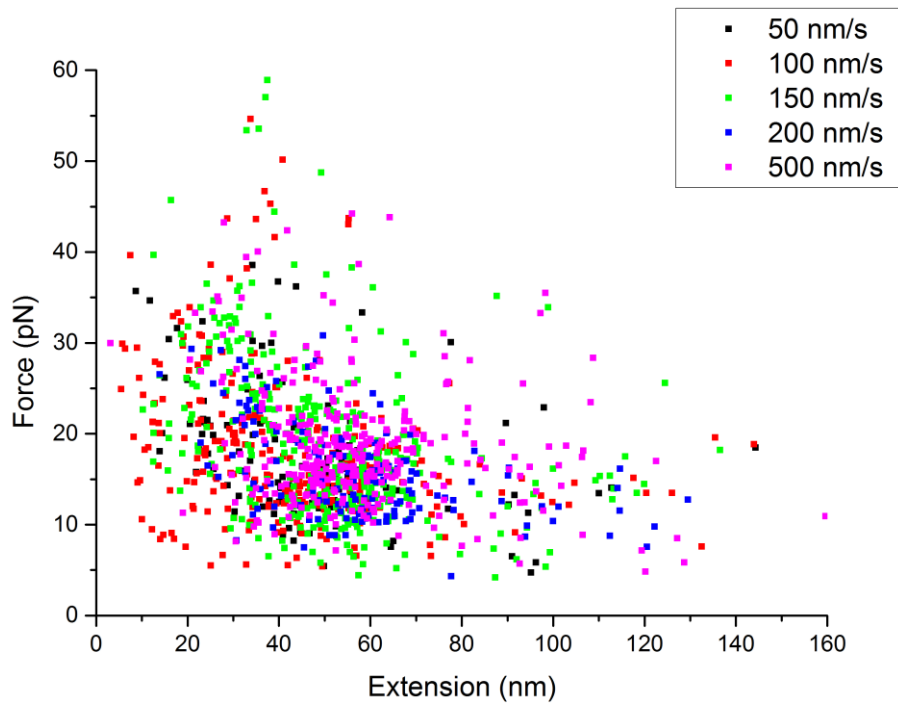
Figure 22 Unfolding events of VWF A2 domain

The unfolding events shown in Fig. 21 are further analyzed by grouping with unfolding forces. Fig. 23 shows the distribution of unfolding events. The highest peak happens in the group of 10 to 20 pN.
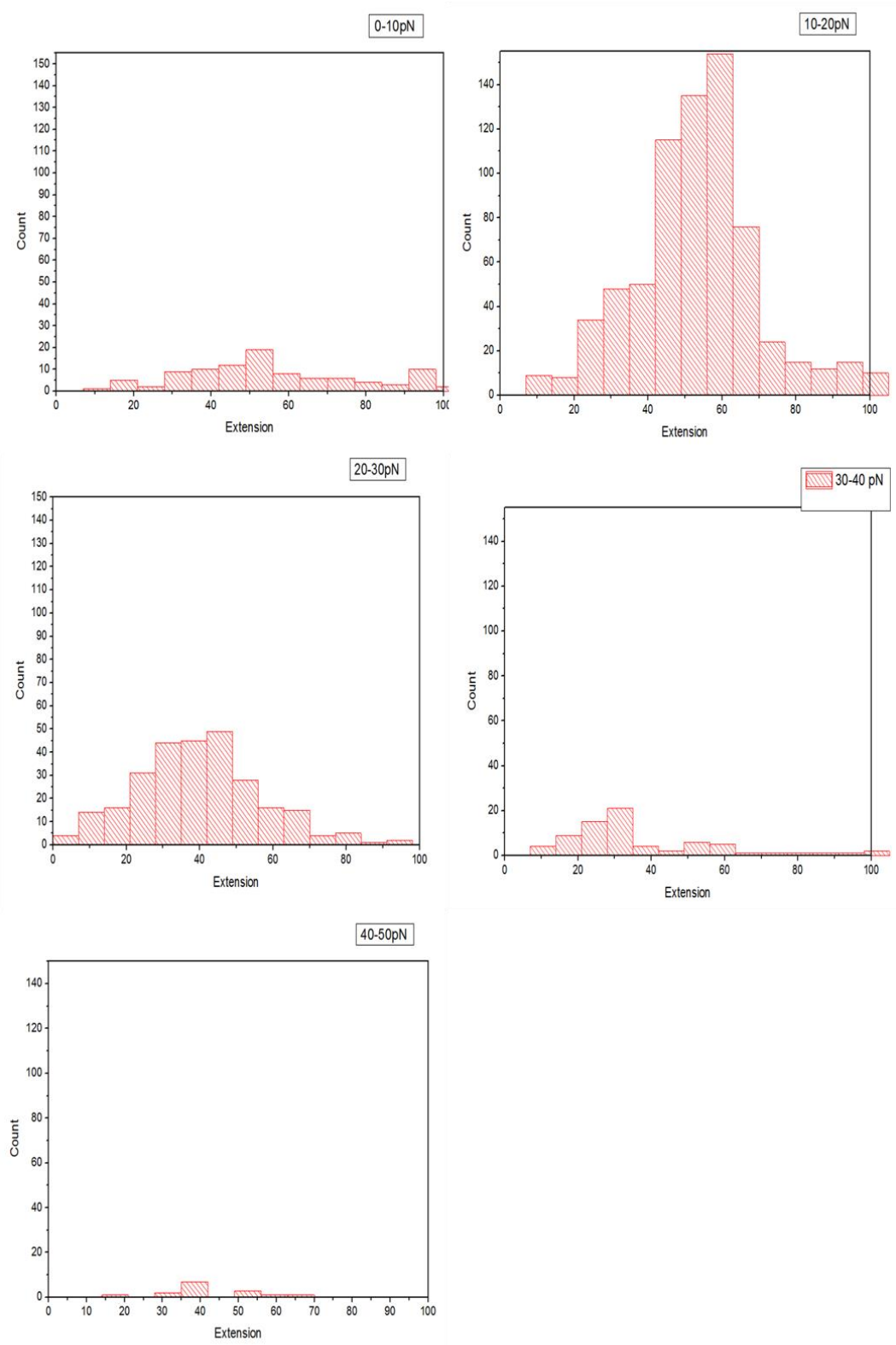
Figure 23 Distribution of VWF A2 domain unfoldings grouped by rapture forces.

3.3 Worm-Like Chain fit for A2 domain of VWF

Wrom-Like Chain model is widely used to describe semi-flexible polymers. It follows the equation, $\frac{FP}{k_BT} = \frac{1}{4}\left(1 - \frac{x}{L_0}\right)^{-2} - \frac{1}{4} + \frac{x}{L_0}$, where F is the external force, x is the extension, P is the persistence length, and L_0 is the contour length. In this study, the external force F and the extension x is achieved directly from the results shown in Fig. 23. Because the simple used in this study is VWF multimer, other domain-domain interaction may also cause a force – extension unfolding. Here, we separate the unfolding events into two groups. The red curve in Fig. 24 is associated with VWF A2 domain unfolding. Comparing with wide type VWF A2 unfolding, mutant Q1541R exhibits similar A2 unfolding trend but has larger extensions. In bloodstream, unfolding of mutant Q1541R requires less hydrodynamic drag force, which makes it easier to be recognized and then cleaved by ADAMTS13. Thus, mutant Q1541R multimer is too short to perform normal platelet binding. The black curve fitted from black blocks associates to less extension is due to VWF D'D3 – A1 interaction. VWF D'D3 – A1 interaction is recently reported and the results here further proved the existence.
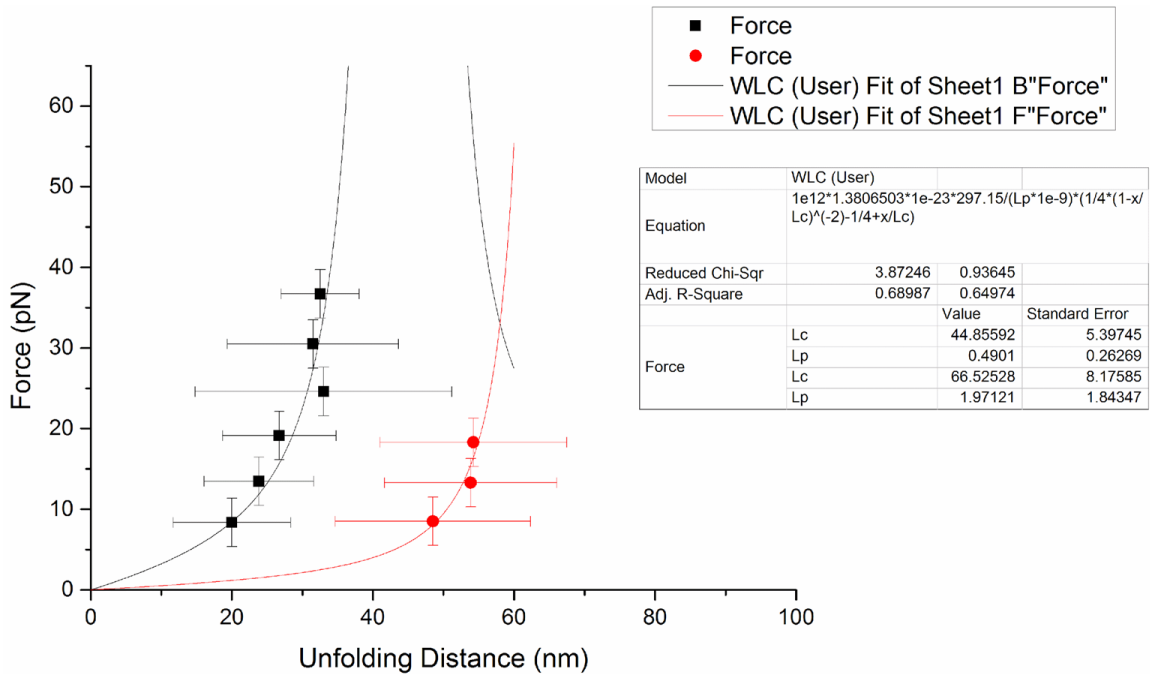
Figure 24 Worm-like chain fitting for VWF D'D3-A1 interaction and A2 unfolding for mutant Q1541R

4. Conclusion

In this chapter, we examined the tensile force and extension associated with A2 domain of VWF mutant Q1541R multimer, a Type 2A mutation, by applying single molecule force spectroscopy experiment. Like other VWD Type 2A, patients with mutant Q1541R has normal quantitate of VWF but mutated to be qualitatively defective. Our result show a larger extension of A2 domain unfolding of VWF mutant 1541, comparing with Wide Type VWD at same level of external force.

CHAPTER 6 *Internal Dynamics of von Willebrand Factor with*

A2 Domain Unfolding

1. Introduction

The A2 domain is capable of significant extension due to hydrodynamic forces experienced in circulation and is therefore represented in this model as a FENE spring. This allows for observed mechanical properties of VWF multimers to be more accurately modelled and permits for the examination of intra-monomer A2 domain unfolding dynamics and subsequent scission by ADAMTS13. VWD Type 2 is a very common type and about 20% of VWD patients have this type. In Type 2 VWD, there usually is enough VWF but it does not work properly, such as multimerization defective and decreased platelet binding. As discussed in early chapters, abnormal mechanism of VWF A2 domain unfolding will cause such defects. When A2 domain requires less force to unfold, the binding and cleavage sites are exposed more frequently and are more likely to stay exposed. Thus, VWF will be cleaved into smaller size distribution than usual, or more collagen binding will perform even at low shear rates. On the other hand, if A2 domain requires larger force to unfold, the binding and cleavage sites are not accessible even at high shear rates.

Previously, this model was used to characterize macromolecular properties such as polymer relaxation and conformation. Here in this chapter, we study the existence of internal tensile force within a VWF molecule in flow and elucidate how this force induces unfolding of the A2 domain. The unfolding of the A2 domain due to force is the primary mechanism for scission and collagen binding, therefore this study aims to quantify the

likelihood and location of binding and cleavage sites for VWF multimers in flow. We examine intra-monomer internal forces for this model and compare our findings to the reported $F \sim N^2$ relationship. Further, we analyze the internal distribution of A2 domain lengths to identify regions where scission is most probable. With this knowledge, we may better understand the banding phenomena observed in healthy circulatory VWF size distributions and have the ability to simulate VWF Type 2A mutant.

2. Simulation Details

Same Brownian molecular dynamics simulations will be performed. We started with an ultra-large VWF multimer ($N = 800$) at shear rate = 1000 per second. Simulation of such large chains are extremely computational expensive. In order to achieve it, a smaller time step is desired. Considering the relaxation time $\tau \sim N^{3/2}$ in HI condition, the time step we used are very from 10^{-5} for $N \leq 60$ beads, 10^{-4} for $N \geq 80$ beads and 10^{-4} for $N \geq 200$ beads. Convergence tests of changing time step are performed before data collection. Shorter length of multimers ($N < 800$) are examined under same flow condition as well. Next, normal length of VWF multimer ($N \leq 200$) are studied under high shear flow, representing the scenario near the injured surface. As discussed in Chapter 4, elongation of molecules exposes more beads on the multimer to interact with collagen binding sites on the surface. A2 domain is treated as unfolded when the length of FENE spring associated has a length of 8 reduced unit and above. In the model we used, if a FENE spring has a length of 8 reduced unit, the tensile force is about 12 pN, which matches the experimental observations. (37) By comparing the difference of A2 domain unfolding, we can further

prove our model is capably to capture the correct internal dynamics and size distribution of VWF multimer.

3. Discussion

From helix parameters, the VWF molecule contains 3500 monomers and will be cleaved by ADAMTS 13 when released into the bloodstream. The presence of shear or elongational flow activates the functional conformation of VWF multimers by a transition between globular and elongated state. (91) Further cleavage by ADAMTS 13 helps the size distribution of VWF reaches homeostasis within 2 hours after released. Usually, the VWF molecular contains up to 40 to 200 monomers. (8) It has been reported that tensile force due to shear or elongation leads to domain unfolding, especially A2 domain. (37) The cleavage sites may not be accessible in equilibrium state or at low shear rates. Defects in A2 domain will cause abnormal cleavages and thus lead to different size distribution. In this chapter, we study large VWF molecular response to flow by examining both the macromolecular unravelling and A2 domain unfolding responses that occur on very different length scales but are crucial for physiological understanding of VWF flow dynamics. The mechanism associated with cleavage by ADAMTS 13 is studied by examining the unfolding properties with different VWF multimer length.

Additionally, defeated in unfolding of A2 domain near injured surface may cause failure of coagulation. Similar to the cleavage sites, the platelets binding sites are shielded by other domains and will be open and exposed to platelets at high shear rates. Thus, the shear induced activation of A2 domain directly affects the VWF collagen binding. In VWD Type 2A, mutated VWF avoids the bond between VWF and platelet. In VWD Type 2B,

however, VWF multimers bind to platelets even at normal flow condition, while lacking both VWF and platelets near the injured. In this chapter, we try to establish a numerical model that is able to simulate different VWF Type 2 mutants under different flow condition. Two separate approaches are performed; ultra-large VWF multimer cleaved by ADAMTS 13 under normal low shear rate flow condition and VWF multimer with homeostasis size distribution near wound under high elongational flow. It would be helpful to understand internal dynamics of A2 domain with a simple coarse grain model that might relate mutations directly to hemostatic dysfunction.

CONCLUDING REMARKS AND OUTLOOK

Von Willebrand Factor (VWF) plays a significant role in coagulation. Decreased production or mutation of VWF will cause von Willebrand Disease (VWD). About 1% of the world population is suffering VWD. In normal condition, VWF is stored in Weibel-Palade bodies (WPB) and can be released to bloodstream when injured. After released, ultra-long VWF multimers are elongated and then cleaved by ADAMTS13 into smaller fragments with mostly 40 to 200 monomers. VWF carries binding sites for both platelets and collagen but may be shielded by other structure and only few is exposing to the blood flow when in a globular state. While at high shear flow field, VWF to an elongated state, more binding sites will be exposed, which enables coagulation. (9)

In this dissertation, a new single molecular VWF model has been presented to study the mechanism of VWF with flow-induced conformational change and collagen binding interaction. It is achieved by modeling VWF monomers as two relatively rigid domains (A1 and A3) connecting by an extendable domain (A2). Zhang et al (37) showed A2 domain of VWF can be completely unfolded with elongational force. Thus, the A2 domain of VWF is modeled as finite extendable non-linear elastic (FENE) springs, and the spring constant is from curve fitting of the results shown reference (37). Between each monomer, a harmonic spring is used to form VWF multimers.

To apply this VWF model, we firstly performed a simply case by initializing the polymer chain to 70% of its maximum length with no flow condition. The results revealed the relaxation time with HI and FD by fitting a power law scaling with number of beads.

The exponents of 1.56 (HI) and 2.08 (FD) agree well with prediction of Rouse and Zimm models. It is shown the length has a profound influence on characteristics of VWF multimer under flow. Longer VWF chain has been proven to have more potential to unfold. The comparison of results for HI and FD showed that HI effect is critical for modeling flow-induced conformational changes of VWF multimer, which hinders unfolding of VWF multimer.

The model is further extended by considering collagen-VWF binding behavior. Collagen binding sites were distributed on the surface homogenously in a square grid with spacing between sites of similar order to spacing between binding sites on model molecules. The A3 domain and collagen interactions were represented by reversible ligand-receptor-type bonds based on Bell model kinetics. The activation energies of unbinding of the Bell model were measured experimentally by force spectroscopy and extracted using the Dudko-Hummer-Szabo model at room temperature. The activation energies of unbinding vary by changing net energy difference from 0 to -3. Brownian dynamics simulations with HI cases show VWF multimer adhesion to the collagen coated surface suppresses dynamic unfolding and refolding. Initially in the model, the results showed a reduction in adhesion probability with increasing flow rate for HI. High adhesion rate regardless flow condition is opposite experimental observations for VWF. To address this, a length threshold was introduced such that, for a given binding site on a model molecule to be able to form either a no-slip bond or a slip bond with a collagen site, the FENE spring adjacent to it was required to be at a length equal to or greater than the threshold. This simple – albeit heuristic – adjustment to our model eliminated the discrepancy with experimentally observed adhesion trends.

Furthermore, internal dynamics of VWF polymer has been studied by examining both the macromolecular unravelling and model A2 domain unfolding responses that occur on very different length scales. We performed the simulations under shear flow for the HI regime. The internal tensile force distribution along a VWF multimer contour has been investigated. The results of ultra-long VWF multimer ($N = 800$) showed more unfolding occur than normal size VWF multimer ($N < 400$) at low shear rate 1000 per second, which has a good agreement to the literature that indicates VWF usually has a length of 40 to 200 monomer after cleaved by ADAMTS 13. Model A2 domains near two multimer ends are the most probable to become unfolded thereby revealing a scissile bond where ADAMTS13 may cleave the chain. Radtke et al (91) showed that tensile force of long polymers exhibits a characteristic double-peak structure. Although more cases with different multimer length are needed, our current results suggested a similar double-peak behavior. With the increasing of shear rate and/or decreasing of multimer length, the double-peak tensile force profile will convert to a hyperbolic structure that force is proportional to the square of length. At high shear rates, the greatest internal tensile force is located at the multimer center. The probability of domain unfolding monotonically increases for multimers of sufficient length. We further illustrated the distributions of internal tensile force for multimers of varying length in the FD regime for the ensemble and only elongated conformations. The results proved that the internal force in multimers scales with the length because longer multimers produce more drag force that must be balanced internally.

The model presented in this dissertation has been proved to have good agreement with experimental results. However, such coarse grain molecule model is not capable of

capturing intra-molecule unfolding: A2 domain unfolding or other domain-domain unfolding. To continue with what have been done here, the future work can be focused on a new method to mimic the intra-molecule unfolding. Besides the FENE spring in the original coarse grain molecule model, another shorter but breakable FENE spring with much larger stiffness can be applied. When molecule is in globule state, both FENE springs are presenting forces to two adjacent beads. With the increasing of the separation between the beads, the short FENE spring is dominating the spring force due to larger stiffness. If the separation increases further, after certain length threshold, the short FENE spring breaks, and then the model converts to the original coarse grain molecule model with only one non-breakable FENE spring. Another possible approach would be applying a Bell model between two adjacent beads connecting by FENE spring. Unlike the VWF collagen binding model used in this dissertation, additional harmonic spring is performed initially and its break is controlled by Bell model. In both methods, the tensile force on A2 domain is the combination of two spring forces before unfolding, and only FENE spring force after unfolding occurs. Furthermore, two methods may be further merged together, using Bell model to control the unfolding and applying FENE spring as the secondary spring before unfolding. Slip bond may also be necessary to obtain a better approximation. With the presence of slip bond, tensile force associates with unfolding can have a relatively large range with most unfolding still occurs around 10 to 15 pN.

Larson et al (56) presented a similar model with spring-spring repulsion, which prevents spring to cross each other. However, instead of a straight spring, the A2 domain of VWF is much more complex and can be highly tangled. When A2 domains of VWF multimer cross each other, the domains may not break but it is possible that the way they

are winding changed. Such details may require a higher model resolution or even a complete different model. Although there is no experimental result on the behavior of multiple A2 domains tangled together, a possible improvement can be focusing on manipulating the unfolding by changing the spring parameters only when a spring-cross has been detected.

BIBLIOGRAPHY

1. Kaushansky, A., J. Allen, and A. Gordus. 2010. Quantifying protein–protein interactions in high throughput using protein domain microarrays. Nat. Protoc. 5: 773–790.

2. Sadler, J.E. 2005. New concepts in von Willebrand disease. Annu. Rev. Med. 56: 173–91.

3. Reviews, C.T. 2009. Outlines & Highlights for Vanders Human Physiology by Eric P. Widmaier. AIPI.

4. Gerritsen, H.E., R. Robles, B. Lämmle, and M. Furlan. 2001. Partial amino acid sequence of purified von Willebrand factor–cleaving protease. Blood. 98.

5. Levy, G.G., W.C. Nichols, E.C. Lian, T. Foroud, J.N. McClintick, B.M. McGee, A.Y. Yang, D.R. Siemieniak, K.R. Stark, R. Gruppo, R. Sarode, S.B. Shurin, V. Chandrasekaran, S.P. Stabler, H. Sabio, E.E. Bouhassira, J.D. Upshaw, D. Ginsburg, and H.-M. Tsai. 2001. Mutations in a member of the ADAMTS gene family cause thrombotic thrombocytopenic purpura. Nature. 413: 488–494.

6. Soejima, K., N. Mimura, M. Hirashima, H. Maeda, T. Hamamoto, T. Nakagaki, and C. Nozaki. 2001. A novel human metalloprotease synthesized in the liver and secreted into the blood: possibly, the von Willebrand factor-cleaving protease? J. Biochem. 130: 475–80.

7. Zheng, X., D. Chung, T.K. Takayama, E.M. Majerus, J.E. Sadler, and K. Fujikawa. 2001. Structure of von Willebrand Factor-cleaving Protease (ADAMTS13), a Metalloprotease Involved in Thrombotic Thrombocytopenic

Purpura. J. Biol. Chem. 276: 41059–41063.

8. Springer, T.A. 2014. Review Article von Willebrand factor , Jedi knight of the bloodstream. 124: 1412–1425.

9. Crawley, J.T.B., R. de Groot, Y. Xiang, B.M. Luken, and D.A. Lane. 2011. Unraveling the scissile bond: how ADAMTS13 recognizes and cleaves von Willebrand factor. Blood. 118: 3212–21.

10. De Meyer, S.F., B. De Maeyer, H. Deckmyn, and K. Vanhoorelbeke. 2009. Von Willebrand factor: drug and drug target. Cardiovasc. Hematol. Disord. Drug Targets. 9: 9–20.

11. Sadler, J.E. 1994. A revised classification of von Willebrand disease. For the Subcommittee on von Willebrand Factor of the Scientific and Standardization Committee of the International Society on Thrombosis and Haemostasis. Thromb. Haemost. 71: 520–5.

12. Nishino, M., and A. Yoshioka. 1997. The revised classification of von Willebrand disease including the previously masqueraded female hemophilia A (type 2N). Int. J. Hematol. 66: 21–30.

13. Edition, T. All About von Willebrand Disease … … for people with von Willebrand disease and their families. .

14. Bird, R.B., C.F. Curtiss, R.C. Armstrong, and O. Hassager. 1987. Dynamics of Polymeric Liquids, Kinetic Theory (Dynamics of Polymer Liquids Vol. 2) (Volume 2). Wiley-Interscience.

15. Perkins, T., and D. Smith. 1995. Stretching of a single tethered polymer in a uniform flow. Sci. YORK …. .

16. Springer, T.A. 2014. Von Willebrand factor, Jedi knight of the bloodstream. Blood. 124: 1412–1425.

17. Yago, T., J. Lou, T. Wu, J. Yang, J.J. Miner, L. Coburn, J. a. López, M. a. Cruz, J.-F.F. Dong, L. V. McIntire, R.P. McEver, and C. Zhu. 2008. Platelet glycoprotein Ibα forms catch bonds with human WT vWF but not with type 2B von Willebrand disease vWF. J. Clin. Invest. 118: 3195–3207.

18. Kim, J., C.-Z. Zhang, X. Zhang, and T. a Springer. 2010. A mechanically stabilized receptor-ligand flex-bond important in the vasculature. Nature. 466: 992–5.

19. Auton, M., C. Zhu, and M.A. Cruz. 2010. The Mechanism of VWF-Mediated Platelet GPIbα Binding. Biophys. J. 99: 1192–1201.

20. Sing, C.E., L. Schmid, M.F. Schneider, T. Franke, and A. Alexander-Katz. 2010. Controlled surface-induced flows from the motion of self-assembled colloidal walkers. Proc. Natl. Acad. Sci. U. S. A. 107: 535–540.

21. Chen, C., P. Depa, V.G. Sakai, J.K. Maranas, J.W. Lynn, I. Peral, and J.R.D. Copley. 2006. A comparison of united atom, explicit atom, and coarse-grained simulation models for poly(ethylene oxide). J. Chem. Phys. 124: 1–11.

22. Westmoreland, P.R., P.A. Kollman, A.M. Chaka, P.T. Cummings, K. Morokuma, M. Neurock, E.B. Stechel, and P. Vashishta. 2002. Applying Molecular and Materials Modeling. Kluwer Academic Publishers.

23. Peterlin, A. 1966. Hydrodynamics of macromolecules in a velocity field with longitudinal gradient. J. Polym. Sci. Part B Polym. Lett. 4: 287–291.

24. Kratky, O., and G. Porod. 2010. Röntgenuntersuchung gelöster Fadenmoleküle.

Recl. des Trav. Chim. des Pays-Bas. 68: 1106–1122.

25.   Rouse, P.E. 1953. A Theory of the Linear Viscoelastic Properties of Dilute

Solutions of Coiling Polymers. J. Chem. Phys. 21: 1272.

26.   Reichert, M. 2006. Hydrodynamic Interactions in Colloidal and Biological

Systems. : 197.

27.   Zimm, B. 1956. Dynamics of polymer molecules in dilute solution: viscoelasticity,

flow birefringence and dielectric loss. J. Chem. Phys. 24: 269–278.

28.   Alexander-Katz, A., M. Schneider, S. Schneider, A. Wixforth, and R. Netz. 2006.

Shear-Flow-Induced Unfolding of Polymeric Globules. Phys. Rev. Lett. 97:

138101.

29.   Sing, C.E., and A. Alexander-Katz. 2010. Elongational flow induces the unfolding

of von Willebrand factor at physiological flow rates. Biophys. J. 98: L35-7.

30.   Rudisill, J. 1993. Brownian-Dynamics Simulation of Chain Models for Dilute

Polymer Solutions in Shear Flow. Comput.

31.   Sing, C.E., J.G. Selvidge, and A. Alexander-Katz. 2013. Von Willlebrand

Adhesion to Surfaces at High Shear Rates Is Controlled by Long-Lived Bonds.

Biophys. J. 105: 1475–1481.

32.   Schneider, S.W., S. Nuschele, A. Wixforth, C. Gorzelanny, A. Alexander-Katz,

R.R. Netz, and M.F. Schneider. 2007. Shear-induced unfolding triggers adhesion

of von Willebrand factor fibers. Proc. Natl. Acad. Sci. U. S. A. 104: 7899–903.

33.   Hernandez-Ortiz, J.P., J.J. de Pablo, and M.D. Graham. 2006. N log N method for

hydrodynamic interactions of confined polymer systems: Brownian dynamics. J.

Chem. Phys. 125: 164906.

34. von Hansen, Y., M. Hinczewski, and R.R. Netz. 2011. Hydrodynamic screening near planar boundaries: Effects on semiflexible polymer dynamics. J. Chem. Phys. 134: 1–15.

35. Hoda, N., and S. Kumar. 2007. Brownian dynamics simulations of polyelectrolyte adsorption in shear flow with hydrodynamic interaction. J. Chem. Phys. 127: 1–15.

36. Hoda, N., and S. Kumar. 2008. Brownian dynamics simulations of polyelectrolyte adsorption in shear flow: Effects of solvent quality and charge patterning. J. Chem. Phys. 128: 1–12.

37. Zhang, X., K. Halvorsen, C.-Z. Zhang, W.P. Wong, and T. a Springer. 2009. Mechanoenzymatic cleavage of the ultralarge vascular protein von Willebrand factor. Science. 324: 1330–1334.

38. Ulrichts, H., M. Udvardy, P.J. Lenting, I. Pareyn, N. Vandeputte, K. Vanhoorelbeke, and H. Deckmyn. 2006. Shielding of the A1 Domain by the D'D3 Domains of von Willebrand Factor Modulates Its Interaction with Platelet Glycoprotein Ib-IX-V. J. Biol. Chem. 281: 4699–4707.

39. Lenting, P.J., J.N. Pegon, E. Groot, and P.G. de Groot. 2010. Regulation of von Willebrand factor-platelet interactions. Thromb. Haemost. 104: 449–455.

40. Karoulia, Z., G. Papadopoulos, M. Nomikos, A. Thanassoulas, T.C. Papadopoulou, G. Nounesis, M. Kontou, C. Stathopoulos, D.D. Leonidas, T. Choli Papadopoulou, G. Nounesis, M. Kontou, C. Stathopoulos, and D. D. Leonidas. 2013. Studies on the Essential Intramolecular Interaction Between the A1 and A2 Domains of von Willebrand Factor. Protein Pept. Lett. 20: 231–240.

41. Baron, R., A.H. de Vries, P.H. Hünenberger, and W.F. van Gunsteren. 2006.

Comparison of Atomic-Level and Coarse-Grained Models for Liquid Hydrocarbons from Molecular Dynamics Configurational Entropy Estimates. : 8464–8473.

42. Kuhn, H., H.-D. Försterling, and D.H. Waldeck. 2009. Principles of Physical Chemistry. John Wiley & Sons.

43. Lankhof, H., M. van Hoeij, M.E. Schiphorst, M. Bracke, Y.P. Wu, M.J. Ijsseldijk, T. Vink, P.G. de Groot, and J.J. Sixma. 1996. A3 domain is essential for interaction of von Willebrand factor with collagen type III. Thromb. Haemost. 75: 950–8.

44. Vickers, J.D. 1999. Binding of polymerizing fibrin to integrin alpha IIb beta3 on chymotrypsin-treated rabbit platelets decreases phosphatidylinositol 4,5-bisphosphate and increases cytoskeletal actin. Platelets. 10: 228–237.

45. Larson, R.G. 2005. The rheology of dilute solutions of flexible polymers: Progress and problems. J. Rheol. 49: 1.

46. Ouyang, W., W. Wei, X. Cheng, X.F. Zhang, E.B. Webb, and A. Oztekin. 2015. Flow-induced conformational change of von Willebrand Factor multimer: Results from a molecular mechanics informed model. J. Nonnewton. Fluid Mech. 217: 58–67.

47. Sundararajan, P.R. 2007. Theta Temperatures. In: Physical Properties of Polymers Handbook. New York, NY: Springer New York. pp. 259–287.

48. Szymczak, P., and M. Cieplak. 2007. Proteins in a shear flow. J. Chem. Phys. 127: 155106.

49. Ermak, D.L., and J. a. McCammon. 1978. Brownian dynamics with hydrodynamic

interactions. J. Chem. Phys. 69: 1352.

50.   Doyle, P., and P. Underhill. 2005. Brownian dynamics simulations of polymers and soft matter. Handb. Mater. Model. : 2619–2630.

51.   Szymczak, P., and M. Cieplak. 2011. Hydrodynamic effects in proteins. J. Phys. Condens. Matter. 23: 33102.

52.   Oseen, C. wihelm. 1927. Hydrodynamik. Akad. Verl.Ges: .

53.   Burgers, J.. 1938. Second Report on Viscosity and Plasticity of the Amsterdam Academy of Sciences. New York: Nordemann.

54.   Rotne, J., and S. Prager. 1969. Variational Treatment of Hydrodynamic Interaction in Polymers. J. Chem. Phys. 50: 4831.

55.   Yamakawa, H. 1970. Transport Properties of Polymer Chains in Dilute Solution: Hydrodynamic Interaction. J. Chem. Phys. 53: 436–443.

56.   Hoda, N., and R.G. Larson. 2010. Brownian dynamics simulations of single polymer chains with and without self-entanglements in theta and good solvents under imposed flow fields. J. Rheol. 54: 1061.

57.   Kubo, R., M. Toda, and N. Hashitsume. 2012. Statistical physics II: nonequilibrium statistical mechanics. .

58.   Sing, C.E., and A. Alexander-Katz. 2011. Equilibrium structure and dynamics of self-associating single polymers. Macromolecules. 44: 6962–6971.

59.   Hsieh, C.-C.C., L. Li, and R.G.G. Larson. 2003. Modeling hydrodynamic interaction in Brownian dynamics: Simulations of extensional flows of dilute solutions of DNA and polystyrene. J. Nonnewton. Fluid Mech. 113: 147–191.

60.   Perkins, T.T.T., D.E. Smith, and S. Chu. 1997. Single polymer dynamics in an

elongational flow. Science. 276: 2016–21.

61. M. Doi and S. F. Edwards. 1986. The theory of polymer dynamics. Oxford University Press Inc.

62. Hur, J.S., E.S.G. Shaqfeh, and R.G. Larson. 2000. Brownian dynamics simulations of single DNA molecules in shear flow. J. Rheol. 44: 713.

63. Tsai, H.-M. 2006. Current concepts in thrombotic thrombocytopenic purpura. Annu. Rev. Med. 57: 419–436.

64. Li, F., J.L. Moake, and L. V. McIntire. 2002. Characterization of von Willebrand factor interaction with collagens in real time using surface plasmon resonance. Ann. Biomed. Eng. 30: 1107–1116.

65. Lisman, T., N. Raynal, D. Groeneveld, B. Maddox, A.R. Peachey, E. G, P.G. De Groot, R.W. Farndale, W. Dc, and E.G. Huizinga. 2006. A single high-affinity binding site for von Willebrand factor in collagen III , identified using synthetic triple-helical peptides Brief report A single high-affinity binding site for von Willebrand factor in collagen III , identified using synthetic trip. Blood. 108: 3753–3756.

66. Huizinga, E.G. 2002. Structures of Glycoprotein Ibalpha and Its Complex with von Willebrand Factor A1 Domain. Science. 297: 1176–1179.

67. Dumas, J.J., R. Kumar, T. McDonagh, F. Sullivan, M.L. Stahl, W.S. Somers, and L. Mosyak. 2004. Crystal structure of the wild-type von Willebrand factor A1-glycoprotein Ibα complex reveals conformation differences with a complex bearing von Willebrand disease mutations. J. Biol. Chem. 279: 23327–23334.

68. Blenner, M.A., X. Dong, and T.A. Springer. 2014. Structural basis of regulation of

von Willebrand factor binding to glycoprotein Ib. J. Biol. Chem. 289: 5565–5579.

69.   Aponte-Santamaría, C., V. Huck, S. Posch, A.K. Bronowska, S. Grässle, M. a Brehm, T. Obser, R. Schneppenheim, P. Hinterdorfer, S.W. Schneider, C. Baldauf, and F. Gräter. 2015. Force-sensitive autoinhibition of the von Willebrand factor is mediated by interdomain interactions. Biophys. J. 108: 2312–21.

70.   Posch, S., C. Aponte-Santamaría, R. Schwarzl, A. Karner, M. Radtke, F. Gräter, T. Obser, G. König, M.A. Brehm, H.J. Gruber, R.R. Netz, C. Baldauf, R. Schneppenheim, R. Tampé, and P. Hinterdorfer. 2016. Mutual A domain interactions in the force sensing protein von Willebrand factor. J. Struct. Biol. 197: 57–64.

71.   Alexander-Katz, A. 2014. Toward Novel Polymer-Based Materials Inspired in Blood Clotting. Macromolecules. 47: 1503–1513.

72.   Ma, H., and M.D. Graham. 2005. Theory of shear-induced migration in dilute polymer solutions near solid boundaries. Phys. Fluids. 17: 1–13.

73.   Serr, A., C. Sendner, F. Müller, T.R. Einert, and R.R. Netz. 2010. Single-polymer adsorption in shear: Flattening vs. hydrodynamic lift and surface potential corrugation effects. Europhys. Lett. 92: 38002.

74.   Sing, C.E., and A. Alexander-Katz. 2011. Non-monotonic hydrodynamic lift force on highly extended polymers near surfaces. Europhys. Lett. 95: 48001.

75.   Dutta, S., K.D. Dorfman, and S. Kumar. 2013. Dynamics of polymer adsorption from dilute solution in shear flow near a planar wall. J. Chem. Phys. 139: 174905.

76.   Dutta, S., K.D. Dorfman, and S. Kumar. 2013. Adsorption of single polymer molecules in shear flow near a planar wall. J. Chem. Phys. 138.

77. Radtke, M., M. Radtke, and R. Netz. 2014. Shear-induced dynamics of polymeric globules at adsorbing homogeneous and inhomogeneous surfaces. Eur. Phys. J. E. Soft Matter. 37: 20.

78. Heidari, M., M. Mehrbod, M.R. Ejtehadi, and M.R.K. Mofrad. 2015. Cooperation within von Willebrand factors enhances adsorption mechanism. .

79. Romijn, R.A., E. Westein, B. Bouma, M.E. Schiphorst, J.J. Sixma, P.J. Lenting, and E.G. Huizinga. 2003. Mapping the collagen-binding site in the von Willebrand factor-A3 domain. J. Biol. Chem. 278: 15035–15039.

80. Farndale, R.W., J.J. Sixma, M.J. Barnes, and P.G. De Groot. 2004. The role of collagen in thrombosis and hemostasis. J. Thromb. Haemost. 2: 561–573.

81. Bell, G.I. 1978. Models for the specific adhesion of cells to cells. Science. 200: 618–627.

82. Evans, E., and K. Ritchie. 1997. Dynamic strength of molecular adhesion bonds. Biophys. J. 72: 1541–55.

83. Dudko, O.K., G. Hummer, and A. Szabo. 2008. Theory, analysis, and interpretation of single-molecule force spectroscopy experiments. Proc. Natl. Acad. Sci. U. S. A. 105: 15755–60.

84. Radtke, M., and R.R. Netz. 2015. Shear-enhanced adsorption of a homopolymeric globule mediated by surface catch bonds. Eur. Phys. J. E. 38: 69.

85. Blake, J.R. 1971. A note on the image system for a Stokeslet in a no-slip boundary. Math. Proc. Cambridge Philos. Soc. 70: 303.

86. Yee, A., and C. Kretz. 2013. von Willebrand Factor: Form for Function. Semin. Thromb. Hemost. 40: 017–027.

87. Xu, A.J., and T. a. Springer. 2013. Mechanisms by which von willebrand disease mutations destabilize the A2 domain. J. Biol. Chem. 288: 6317–6324.

88. Batlle, J., M. Lopez-Fernandez, A. Lopez-Borrasca, C. Lopez-Berges, J. Dent, S. Berkowitz, Z. Ruggeri, and T. Zimmerman. 2016. Proteolytic degradation of von Willebrand factor after DDAVP administration in normal individuals. Blood. 70: 173–176.

89. Wilson, L., P. Matsudaira, and M. Sheetz. 1997. Laser tweezers in cell biology. .

90. Smith, S., Y. Cui, and C. Bustamante. 2003. Optical-trap force transducer that operates by direct measurement of light momentum. Methods Enzymol. .

91. Radtke, M., S. Lippok, J.O. Rädler, and R.R. Netz. 2016. Internal tension in a collapsed polymer under shear flow and the connection to enzymatic cleavage of von Willebrand factor. Eur. Phys. J. E. 39: 32.

VITA

Wei Wei was born on Friday, June 8, 1985 in Shanghai, China. His father is Luguang Wei and mother Ling Liang. Wei attended Shanghai Weiyu High School, where his passion for math and science got excited. He graduated from high school in June of 2003. Wei enrolled at Shanghai Jiao Tong University in September of 2003 and received his Bachelor of Science in Mechanical Engineering degree in July 2007. In August 2009, Wei went to Lehigh University in Bethlehem, Pennsylvania. There, he worked on multiple research projects, including Mechano-Biologically Informed Molecular Models of Flow Sensitive Biopolymers and Portable Micro-Hydroturbine Power System. He received his Master of Science in Mechanical Engineering degree in December 2012 with a 3.8 grade point average. Wei pursued his doctoral degree and received in August 2017.